

HEALTH AND MEDICINE

Targeting and arginine-driven synergizing photodynamic therapy with nutritional immunotherapy nanosystems for combating MRSA biofilms

Aoxue Zhang¹, Hao Wu², Xin Chen¹, Zhen Chen³, Yuanhu Pan³, Wei Qu³, Haihong Hao¹, Dongmei Chen^{3*}, Shuyi Xie^{1,2,3*}

The resistance and immune escape of methicillin-resistant *Staphylococcus aureus* (MRSA) biofilms cause recalcitrant infections. Here, we design a targeting and synergizing cascade PDT with nutritional immunotherapy nanosystems (Arg-PCN@Gel) containing PCN-224 as PDT platform for providing reactive oxygen species (ROS), incorporating arginine (Arg) as nitric oxide (NO) donor to cascade with ROS to produce more lethal ONOO⁻ and promote immune response, and coating with gelatin as targeting agent and persistent Arg provider. The nanosystems adhered to the autolysin of MRSA and inhibited Arg metabolism by down-regulating *icdA* and *icaA*. It suppressed polysaccharide intercellular adhesion and extracellular DNA synthesis to prevent biofilm formation. The NO broke mature biofilms and helped ROS and ONOO⁻ penetrate into biofilms to inactivate internal MRSA. Arg-PCN@Gel drove Arg to enhance immunity via inducible NO synthase/NO axis and arginase/polyamine axis and achieve efficient target treatment in MRSA biofilm infections. The targeting and cascading PDT synergized with nutritional immunotherapy provide an effective promising strategy for biofilm-associated infections.

INTRODUCTION

Staphylococcus aureus is one of the most common organisms responsible for hospital-acquired bacterial infections including osteomyelitis, pulmonary infections, and endocarditis (1–3). In the United States, approximately 20,000 deaths every year from *S. aureus* bacteremia already exceed the combined deaths from acquired immunodeficiency syndrome, tuberculosis, and viral hepatitis. The prevalence rise of methicillin-resistant *S. aureus* (MRSA) further aggravates the threat. Biofilms are an important virulence factor and resistance mechanism of MRSA (4). The sticky and dense extracellular polymer (EPS) mainly including extracellular DNA (eDNA), polysaccharides, and glycoproteins of biofilms not only defends MRSA from the host's immune attack but also blocks the killing of MRSA inside biofilms by antibiotics, resulting in serious and persistent inflammation, treatment challenges and recalcitrant infections (5). Some MRSA embedded in biofilms present in the inactive metabolic state is over 1000-fold more resistant to antibiotics than their planktonic counterparts and thus renders antibiotics ineffective (6). Thus, there is an urgent need to develop a multifunctional treatment strategy with synergistic antimicrobial therapy and immunotherapy to effectively combat MRSA biofilms (7–9).

Photodynamic therapy (PDT) stemmed from photosensitizers (PSs), which uses oxygen (O₂) to generate reactive oxygen species

(ROS; such as ¹O₂) under irradiation to destroy bacteria structures, is considered a promising new therapy strategy for biofilms (10, 11). However, clinically approved PSs (e.g., porphyrins and their derivatives) suffer from low ROS yields due to their aggregation in aqueous solutions (12). To solve this problem, some new PSs were explored for aggregation-induced emission (AIE) that enhances ROS production during aggregation (13, 14). For example, Wang *et al.* (14) developed effective quaternary amine functionalized AIE nanoparticles with excellent antibacterial properties against *S. aureus* and *Escherichia coli*. More lethal, EPS of biofilms can block the penetration of PSs, and a large number of antioxidant substances (e.g., glutathione and superoxide dismutase) in biofilms can consume ROS free of charge to reduce the efficiency of PDT (15). Besides, the poor selectivity and short diffusion property of ROS (100 nm in aqueous solution) also limit the lethality of PDT to bacteria and nonspecifically destroy the host cells (12). They cannot trigger an immune response to enhance tissue healing from the pro-inflammatory stage to the anti-inflammatory stage. Thus, effective PDT therapy in vivo requires targeting recognition and good penetration across biofilms to maintain effective antibacterial concentration to combat MRSA outside and inside biofilms and simultaneous stimulating moderate immune response. Metal-organic framework (MOF) is a controlled, ordered, and coordinated porous structure formed by metal nodes and organic ligands (16). It is reported that nanoscale MOF has the advantages of large specific surface area and fast energy transfer due to the synergism and periodic structure of metal joint bridging units of PSs, which can optimize the light capture and penetration ability of PSs (16, 17). Compared to other nanomaterials, the notable advantage of MOF is to use PSs as its components rather than encapsulation or adsorption. Therefore, the premature release of PSs can be largely avoided en route. Unfortunately, they can still not effectively overcome

Copyright © 2023 The Authors, some rights reserved; exclusive licensee American Association for the Advancement of Science. No claim to original U.S. Government Works. Distributed under a Creative Commons Attribution NonCommercial License 4.0 (CC BY-NC).

¹National Key Laboratory of Agricultural Microbiology, Huazhong Agricultural University, Wuhan, Hubei 430070, China. ²National Reference Laboratory of Veterinary Drug Residues (HZAU) and MAO Key Laboratory for Detection of Veterinary Drug Residues, Wuhan, Hubei 430070, China. ³Key Laboratory of Prevention & Control for African Swine Fever and Other Major Pig Diseases, Ministry of Agriculture and Rural Affairs, Wuhan, Hubei 430070, China.

*Corresponding author. Email: dmchen1027@163.com (D.C.); snxsy1@126.com (S.X.)

active oxygen consumption, possible nonspecific toxicity of active oxygen to host cells, and immune escape of biofilm-embedding bacteria.

The arginine (Arg) catabolic mobile element (ACME-arc) of MRSA inside biofilms is highly expressed in aerobic or hypoxic environments, competing with host immune cells to use Arg to thrive and suppress the immune response at the infected site (18–20). Simultaneously, Arg is an important nutrient medium for triggering the host immune response during initial inflammation and subsequent resolution (21). Host cells compete with bacteria for Arg to produce nitric oxide (NO) through inducible nitric oxide synthase (iNOS) (iNOS/NO axis) during the pro-inflammatory phase to achieve enhanced antibacterial activity and immune response (21, 22). Meanwhile, arginase (Arg-1) can convert Arg into polyamines (Arg-1/polyamine axis) in the anti-inflammatory phase to promote wound healing. Therefore, additional Arg supplementation will help enhance the host's immune response. It is interesting that Arg can produce NO and citrulline under the action of $^1\text{O}_2$ and the citrulline can be resynthesized to Arg by host cells to realize its recycling (22, 23). Moreover, NO can deplete oxidative substances in biofilms and generate peroxynitrite anion (ONOO^-) with ROS even under extremely low concentrations ($>1 \mu\text{M}$), to which bacteria are more sensitive, thereby synergistically enhancing the anti-biofilm effect of ROS (15, 24–26). It is reported that gelatin has the ability to selectively adhere autolysin (*atl*, a staphylococcal cell surface multifunctional protein) of *S. aureus* (27). Fortunately, the overexpressed matrix metalloproteinases (MMPs) of *S. aureus* can degrade gelatin to release Arg at the infected site (28, 29). Thus, these potential abilities of Arg, gelatin, and PSs-based MOF encourage us to develop a combination and multifunctional strategy that allows targeting and Arg-driven cascading and synergizing PDT with immunotherapy for expected highly efficacious combating MRSA biofilms.

Here, a targeting nanosystem (Arg-PCN@Gel) was designed for effective prophylaxis and therapy of MRSA biofilm infections with cascading and synergizing PDT and nutritional immunotherapy (Fig. 1). The core PCN-224 was prepared by PS of meso-tetrakis(4-carboxyphenyl)porphyrin (TCPP) and metal zirconium (Zr) to enhance the biofilms penetration and light capture capacity. Arg was doped into PCN-224 to form Arg-PCN to achieve the cascading and synergizing effects of $^1\text{O}_2$ and NO as well as to enhance the immune response of the host. Last, Arg-PCN was covered with hydrophilic gelatin to provide targeting delivery performance and persistent Arg donor. The Arg-PCN@Gel can target MRSA mediated by *atl* and then release the core Arg-PCN via overexpressing of MMPs at the infection sites. Under irradiation, the nanosystems can produce different active substances of ROS, NO, and ONOO^- in cascade reaction and stimulate Arg-enhanced immunity to synergistically prevent and treat biofilms. The nanosystems suppressed MRSA Arg and element metabolism, energy usage efficiency, two-component systems, and EPS synthesis to prevent biofilms formation by down-regulating *cidA*, *icaA*, *arsR*, *copZ*, *codY*, *ccpA*, and others. It used NO to effectively break mature biofilms barrier to help ROS and ONOO^- penetrate into biofilms to damage internal MRSA cell walls and membranes. Simultaneously, the firstly produced low level of NO by Arg-PCN@Gel under the irradiation induced the pro-inflammatory factor of TNF- α (tumor necrosis factor- α) and iNOS expression and further used Arg to produce a large amount of NO for achieving antibacterial effects.

Subsequently, the gradually accumulated NO not only cleared bacteria but also induced the anti-inflammatory factor of interleukin-4 (IL-4) and Arg-1 expression, thereby using Arg to promote wound healing by the transformation of infected tissue from the pro-inflammatory stage to the anti-inflammatory stage. The Arg-PCN@Gel will be a novel promising effective way to fight against biofilm-associated infections.

RESULTS AND DISCUSSION

Design and characterization of Arg-PCN@Gel

This study was the first to synthesize the targeting multifunctional nanosystems (Arg-PCN@Gel) with Arg-driven cascading PDT coordinated with nutritional immunotherapy (Fig. 2A). The core PCN-224 was formed by self-assembly of the carboxyl of TCPP and Zr clusters, confirmed by characteristic diffraction peaks of PCN-224 in the powder x-ray diffraction pattern (Fig. 2B), oscillation peaks of Zr-OH and phenyl in the Fourier transform infrared spectrum (FTIR) (Fig. 2C), and ultraviolet-visible (UV-Vis) spectra of TCPP (Fig. 2H) (30–32). To promote oxidation and Arg-triggered immune response, Arg-PCN was synthesized on the basis of PCN-224 by a hot solvent method. The carboxyl of Arg competed with TCPP in PCN-224 for Zr clusters to perform ligand replacement to form a disordered crystalline phase, which was verified by the FTIR absorption peaks of primary and secondary amine at 2800 to 3300 cm^{-1} (Fig. 2C), decreased zeta potential (ZP) from $+17.9 \pm 2.8 \text{ mV}$ to $-23.4 \pm 1.1 \text{ mV}$ (Fig. 2D) and UV-Vis spectra of Arg (Fig. 2H). The disappeared C=N characteristic peaks of Arg (1670 cm^{-1}) may be related to the overlapping of the COO^- symmetric and asymmetric stretching vibrational peaks of PCN-224 at 1400 and 1610 cm^{-1} . The dispersibility and surface hydrophilicity of Arg-PCN were improved after coating with hydrophilic gelatin by using Ca^{2+} as cross-linking agent (Fig. 2, E to G). The gelatin encapsulation was confirmed by the gelatin hydroxyl oscillation peak appeared at 1080 cm^{-1} (Fig. 2C), appeared UV-Vis spectra of gelatin (Fig. 2H), similar potential to gelatin solution ($-11.3 \pm 3.1 \text{ mV}$) (Fig. 2D), and decreased contact angles of Arg-PCN@Gel (Fig. 2G). The gradual increase in the hydrodynamic and true size of the three spherical PCN-224, Arg-PCN, and Arg-PCN@Gel nanosystems determined by photon correlation spectroscopy (Fig. 2I and table S1), scanning electron microscope (SEM) (Fig. 2E), and transmission electron microscope (TEM) (Fig. 2F) also indicates the successful incorporation of Arg and coating of gelatin.

Red light-triggered ROS and its cascading products of NO and ONOO^-

On-demand delivery of the nanosystems in response to specific expressed MMPs in MASR infection microenvironment and the exogenous red light was evaluated to show its therapy enhancement (Fig. 3A). The $^1\text{O}_2$ and total ROS production efficiency of our designed nanosystems under 660-nm light irradiation was tested by singlet oxygen fluorescent probe (SOSG) and dichlorodihydrofluorescein diacetate (DCFH-DA) probe, respectively. The two-fluorescence probe intensity of PCN-224, Arg-PCN, and Arg-PCN@Gel at the same concentrations of TCPP was similar, indicating that $^1\text{O}_2$ and total ROS production efficiency of TCPP is not weakened by Arg incorporation and gelatin covering (Fig. 3, B and E). The $^1\text{O}_2$ and total ROS generation performance of Arg-PCN@Gel showed

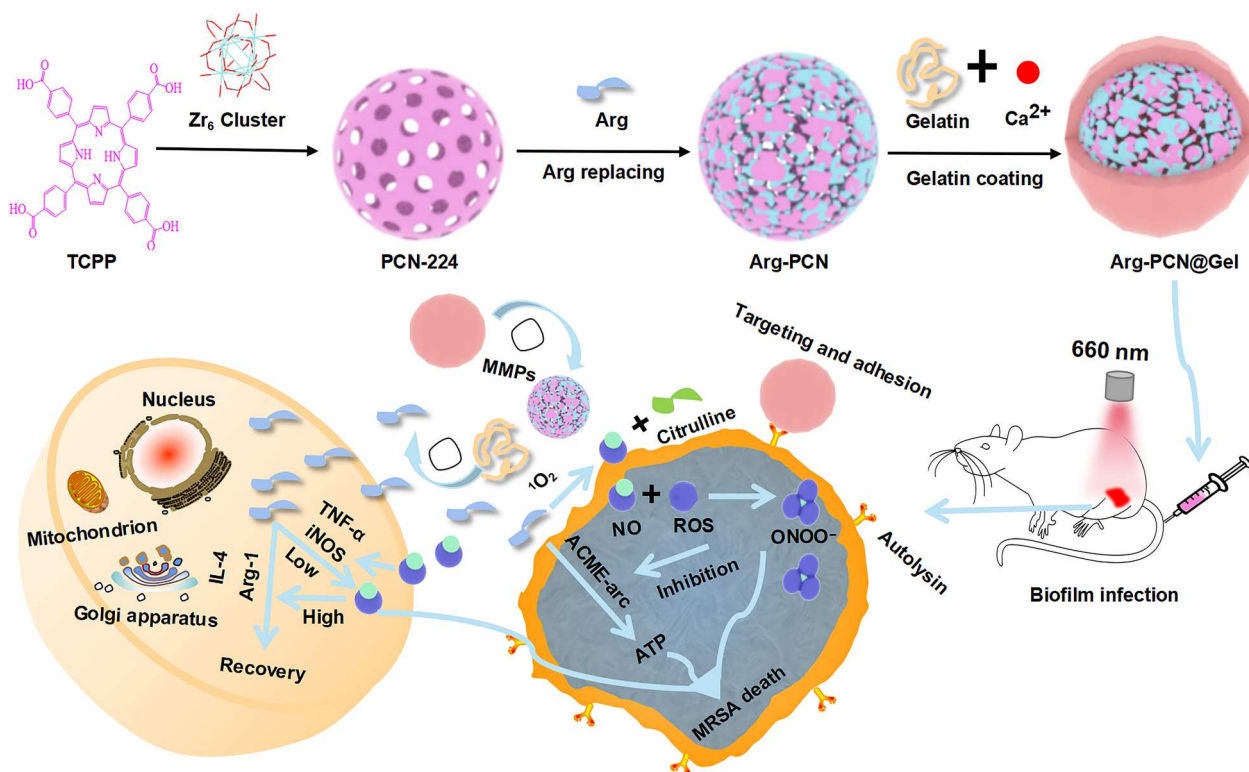


Fig. 1. Schematic diagram of Arg-PCN@Gel preparation and targeted synergistic PDT and nutritional immunotherapy in vivo. PCN-224 was formed by a hot solvent method, followed by ligand substitution with Arg to form Arg-PCN, which was lastly encapsulated in gelatin to form Arg-PCN@Gel. Arg-PCN@Gel can target biofilm-infected sites by intravenous administration and can target MRSA that adhered to the infected site by autolysin; gelatin was degraded by MMPs at the site of infection to produce Arg. Under 660-nm laser irradiation, Arg-PCN@Gel cascaded to produce a large number of active substances (ROS, NO, and ONOO⁻), which can not only damage the cell wall and membrane of MRSA but also inhibit the competition between MRSA and the host for Arg. In addition, NO has a bidirectional regulatory effect, which can promote the production of pro-inflammatory factors at low concentrations to resist MRSA infection. At high concentrations, it promoted the host's transition from the pro-inflammatory stage to the anti-inflammatory stage and promotes tissue recovery. TCPP, meso-tetrakis(4-carboxyphenyl) porphyrin; IL-4, interleukin-4; TNF- α , tumor necrosis factor- α ; ATP, adenosine 5'-triphosphate.

time and concentration-dependent characteristics (Fig. 3, C and F). Concurrently, the intracellular ROS produced by the nanosystem was also detected. Compared to the control group, PCN-224, Arg-PCN, and Arg-PCN@Gel could more significantly produce ROS under irradiation and be used for subsequent treatment (Fig. 3D). Compared with ROS that nonspecifically induces apoptosis and necrosis, NO can prevent oxidative damage of host cells and produce ONOO⁻ for stronger inactivation of bacteria (24, 33). Arg that can generate NO under the action of ¹O₂ and iNOS was incorporated into PCN-224. In addition, the covered gelatin could be decomposed to produce Arg under the action of MMPs secreted by MRSA (Fig. 3G) to enhance NO and ONOO⁻ production (28, 29). Thus, the NO and ONOO⁻ were quantitatively detected by using Griess reagent and L-tyrosine as indicators, respectively. The Arg-PCN showed similar NO yields of 3.97 μ M as the equivalent concentration of Arg-PCN@Gel (3.54 μ M) after irradiation without MMPs, while the NO yields of Arg-PCN@Gel were increased to 5.31 μ M when incubating with MMPs (Fig. 3, H and I, and fig. S1) (34). The NO also exhibited a concentration and time dependence as ¹O₂ under irradiation and MMP responsiveness (Fig. 3I). The ONOO⁻ produced by Arg-PCN@Gel incubating with MMPs was 1.25 and 11 times that of Arg-PCN and PCN-

224, respectively (Fig. 3J). The ONOO⁻ produced by PCN-224 was negligible.

Safety evolution and activity against planktonic MRSA

The cytotoxicity of our designed nanosystems was assessed by the vitality, membrane integrity, and morphology change of NIH/3T3 cells to determine the irradiation time. The PCN-224, Arg-PCN, and Arg-PCN@Gel did not show any cytotoxicity in the dark and under red light irradiation for 0 and 10 min, and the cell viability after treatment with different nanosystems is higher than 100% (Fig. 4, A and B, and figs. S2 and S3). This may be related to Zr⁴⁺ in nanosystems, which can promote the proliferation and differentiation of osteoblasts and can be used as a substitute material for bone transplantation (35, 36). ZrO₂ is also reported to promote the proliferation of fibroblasts and facilitate tissue healing (37). The lactate dehydrogenase (LDH) activity was maintained at about 100%, suggesting that the increased cell viability by the Arg-PCN@Gel does not induce cytotoxicity. After 20 min of irradiation, PCN-224 and Arg-PCN exhibited obvious cytotoxicity at concentrations above 8 and 32 μ g ml⁻¹, respectively. The NIH/3T3 cells were changed from normal fibroblast-like to round when treated with PCN-224 and Arg-PCN (32 μ g ml⁻¹) over 20-min irradiation, respectively (Fig. 4C and fig. S4). Arg-PCN@Gel

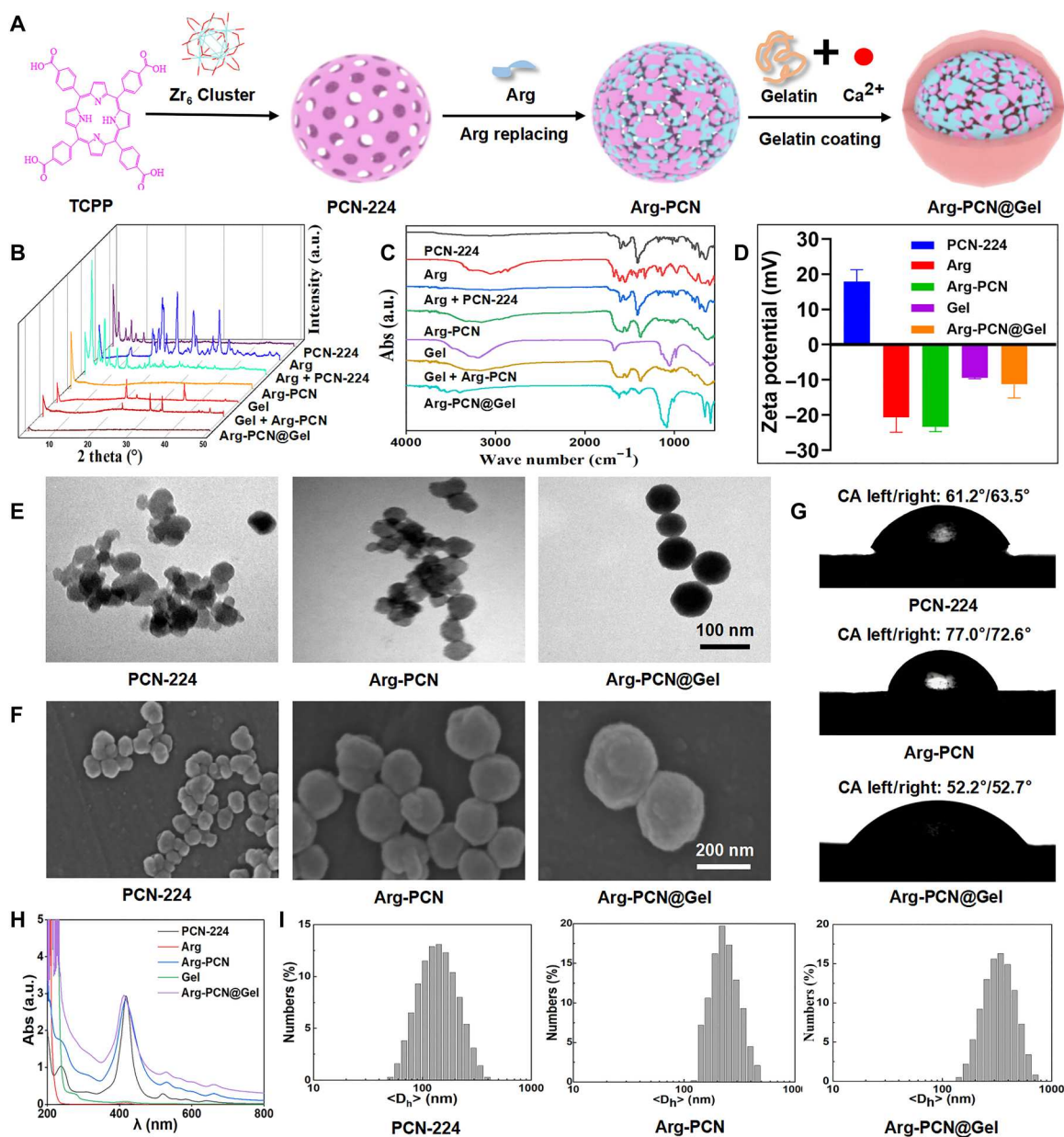


Fig. 2. Preparation and characterization of Arg-PCN@Gel. (A) Schematic diagram of Arg-PCN@Gel preparation. (B to D) Powder x-ray diffraction (B), Fourier transform infrared (C), and zeta potential (D) of PCN-224, Arg-PCN, Arg-PCN@Gel, Arg, and gelatin. (E) Transmission electron microscopy (TEM) images. (F) Scanning electron microscopy (SEM) images. (G to I) Water drop contact angles (G), ultraviolet-visible spectrum (H), and size distribution (I) of PCN-224, Arg-PCN, and Arg-PCN@Gel. a.u., arbitrary units.

still did not lead to cell viability and morphological change (Fig. 4, A and C). Its reduced cytotoxicity is as we expected possibly due to more hydrophilicity and NO produced by $^1\text{O}_2$ -catalyzed Arg (Figs. 2G and 3E) (23). Under this treatment condition, the cell viability and LDH activity were $114.73 \pm 1.45\%$ and $97.01 \pm 5.17\%$, respectively. When the Arg-PCN@Gel concentration was increased to $32 \mu\text{g ml}^{-1}$, although the LDH activity increased to $117.50 \pm 5.23\%$, the cell viability was still kept at $98.07 \pm 3.79\%$ (Fig. 4, A and B). These results suggest that our designed Arg-PCN@Gel has good safety and the irradiation time of therapy should not exceed 30 min. Incorporation of Arg and coating of hydrophilic

gelatin also greatly increased biocompatibility. The PCN-224 caused a $16.09 \pm 0.39\%$ hemolysis rate at 4 mg ml^{-1} , while the hemolysis rate of Arg-PCN and Arg-PCN@Gel was lower than the recognized standard (5%) even up to 10 mg ml^{-1} (fig. S5).

On the basis of cytotoxicity and biocompatibility, the light irradiation time was further optimized via sensitive tests. The antibacterial activity of different nanosystems against two clinic strains of MRSA (B1-1 and P1-2) was enhanced with the increase of irradiation time within 30 min and significantly increased by incorporation of Arg and coating of gelatin (Fig. 4D and fig. S6). Compared to PCN-224 and Arg-PCN, the minimum bactericidal concentration

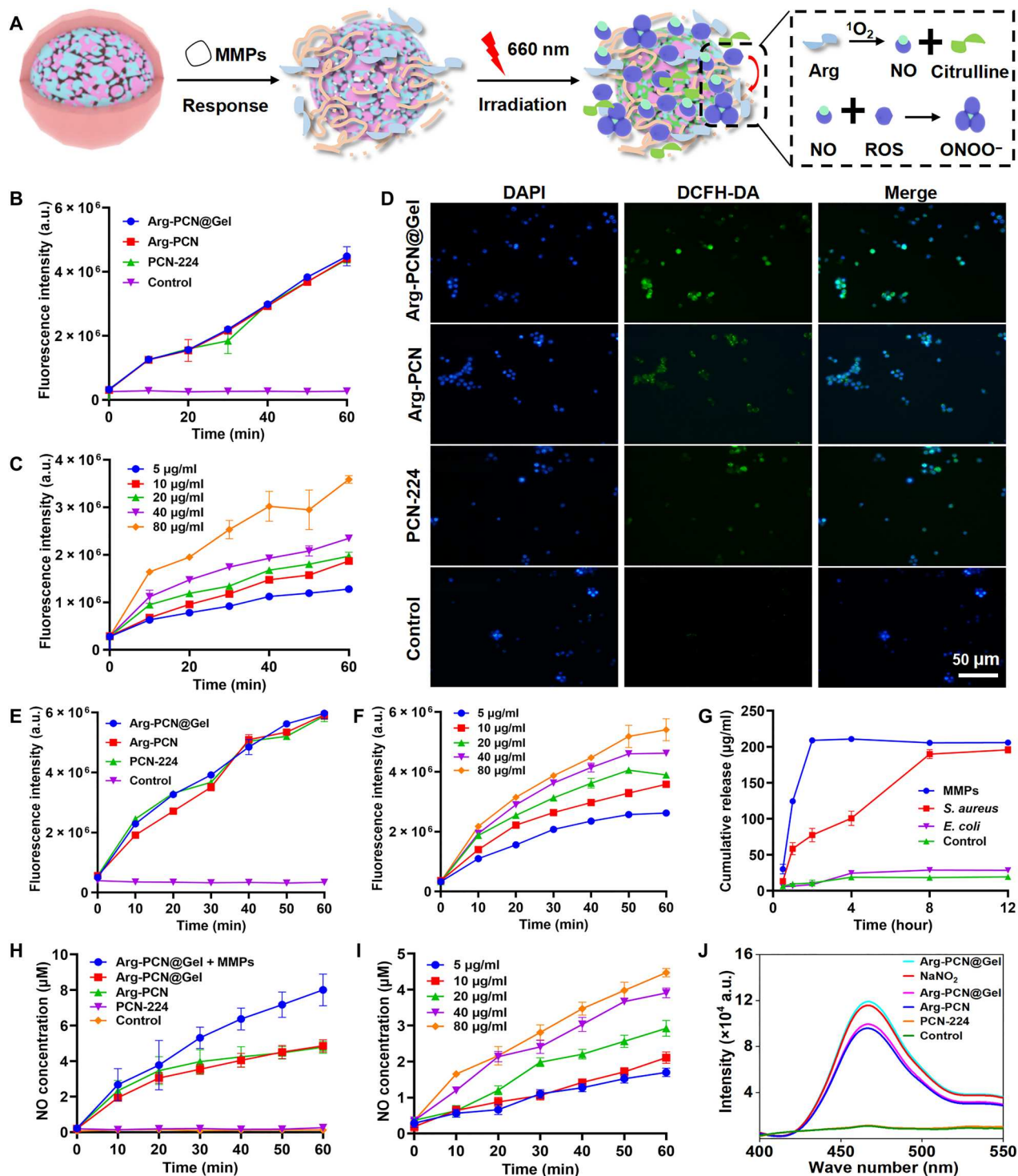


Fig. 3. Red light mediated the cascade reaction of Arg-PCN@Gel. (A) Cascading reaction of Arg-PCN@Gel. (B) ROS produced by different nanosystems under irradiation at different times. (C) ROS produced by different concentrations of Arg-PCN@Gel under irradiation. (D) Fluorescence images of intracellular generation ROS under irradiation. (E) 1O_2 produced by different nanosystems under irradiation at different times. (F) 1O_2 produced by different concentrations of Arg-PCN@Gel under irradiation. (G) Cumulative release of Arg. (H) NO produced by different nanosystems under irradiation at different times. (I) NO produced by different concentrations of Arg-PCN@Gel under irradiation. (J) ONOO⁻ produced by different nanosystems under irradiation. DAPI, 4',6-diamidino-2-phenylindole; DCFH-DA, dichlorodihydrofluorescein diacetate.

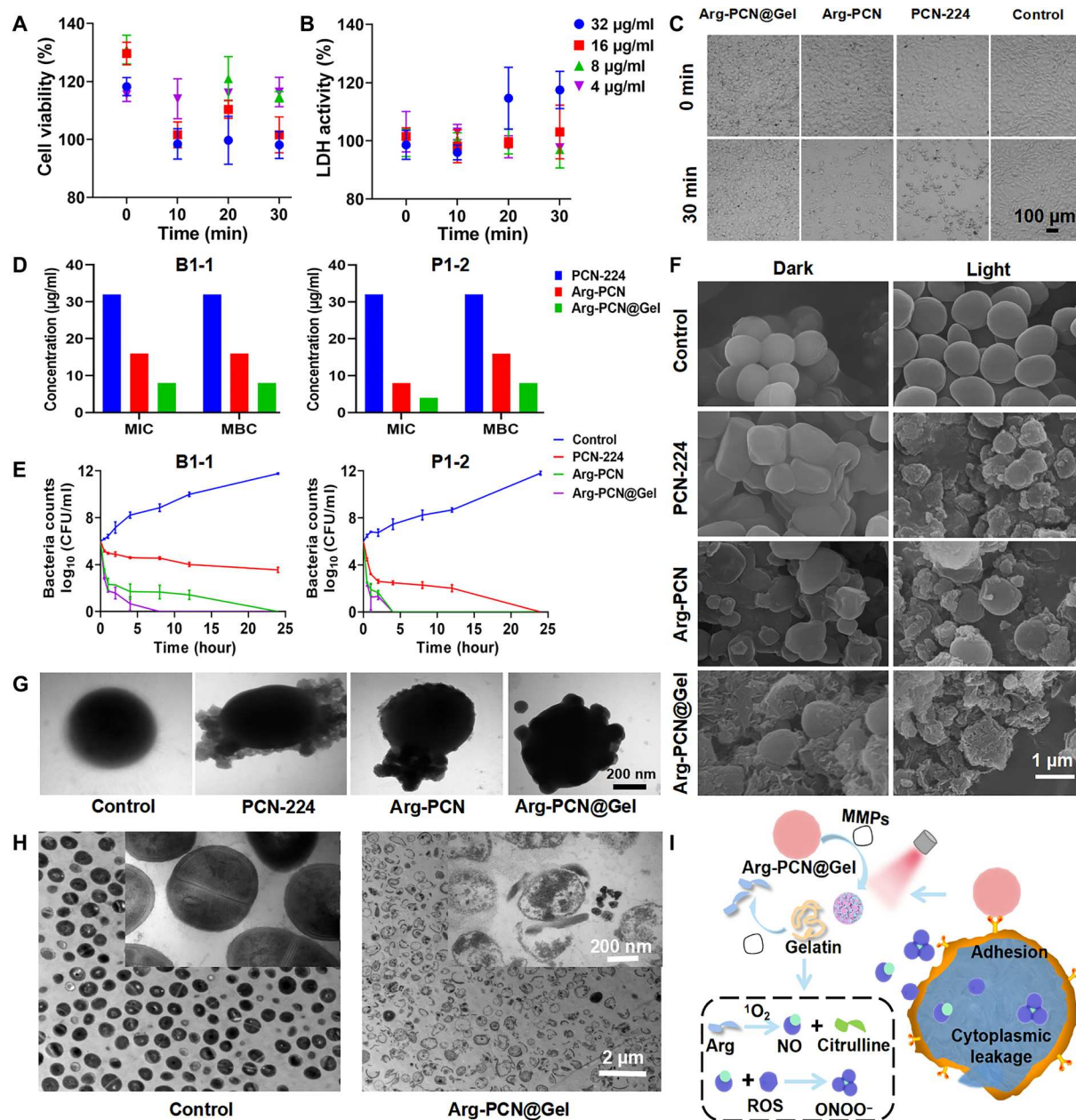


Fig. 4. Antibacterial properties of Arg-PCN@Gel. (A to C) Under different irradiation times, viability (A), cell membrane integrity (B), and morphology (C) (scale bar, 100 µm) of cells treated with different nanosystems for 24 hours. (D and E) minimum inhibitory concentration (MIC), minimum bactericidal concentration (MBC) (D), and bactericidal curves (E) of different nanosystems against MRSA (B1-1 and P1-2), respectively. (F) SEM images of MRSA (B1-1) after treatment with different nanosystems in the absence or presence of irradiation. (G) Interaction of different nanosystems with MRSA (B1-1) surface in the absence of irradiation observed by TEM. (H) Cell structure TEM images of MRSA (B1-1) treated with Arg-PCN@Gel under irradiation. (I) Antibacterial mechanism of NO-enhanced PDT-based Arg-PCN@Gel after irradiation.

(MBC) and minimum inhibitory concentration (MIC) of Arg-PCN@Gel against both clinical strains of MRSA were smallest and their MBC/MIC ratios were both ≤ 4 , presenting a bactericidal advantage and fast sterilization rate (Fig. 4, D and E, and fig. S7) (38). The designed nanosystems could adhere to MRSA to change MRSA morphology from smooth and round spherical to irregular in the dark (Fig. 4, F and G) and more severe deformation under irradiation after treating with MBC (deformation severity:

Arg-PCN@Gel > Arg-PCN > PCN-224) (Fig. 4, F and H). The significant discrepancy of MRSA morphology in dark and under irradiation indicates that nanosystems can destroy bacterial cell walls and membranes by producing a large amount of ROS and its cascade-generated NO and ONOO⁻ with Arg (Fig. 4I) (15, 39). The strongest antibacterial activity of Arg-PCN@Gel is due to the best hydrophilicity (Fig. 2G) to sufficiently use light energy without aggregations, targeting adhesion (Fig. 4G) to MRSA surfaces to facilitate the killing efficiency of ROS with a short diffusion distance

and the persistent generation of Arg to cascade-generate enough NO and ONOO⁻ (Figs. 3G and 4I) (12).

Prophylaxis and eradication effects against biofilms and its embedded MRSA

The three different nanosystems all exhibited dose-dependent activity against the formation of biofilm both in the dark and under irradiation (Fig. 5, A and B, and figs. S8 and S9). Under irradiation, 4 $\mu\text{g ml}^{-1}$ of vancomycin (considered as the last defense line for treating MRSA), Arg-PCN@Gel, Arg-PCN, and PCN-224 could reduce 82.36 \pm 1.14%, 71.47 \pm 6.48%, 57.44 \pm 7.09%, and 45.08 \pm 4.21% biofilms formation (B1-1), respectively (Fig. 5A). At the concentrations of 4 and 8 $\mu\text{g ml}^{-1}$, PCN-224 had no significant effect on both biofilm formation and bacterial viability of B1-1 and P1-2 in dark and under irradiation, while the other two groups of Arg-PCN@Gel and Arg-PCN had significant difference. The possible reasons for the no significant difference at the low concentration are due to its own anti-biofilm activity of TCPP and the produced less and single active substances by PCN-224 after irradiation. When the concentration was increased to 32 $\mu\text{g ml}^{-1}$, the biofilm inhibition effect of Arg-PCN@Gel was equal to vancomycin. Simultaneously, the viability of B1-1 and P1-2 was decreased to 8.50 \pm 2.66% and

5.96 \pm 4.04% by Arg-PCN@Gel (Fig. 5B). The Arg-PCN@Gel inhibited the formation of biofilms by destroying polysaccharides and eDNA (Fig. 5, C and D, and figs. S10 and S11) (40). The inhibitory effects of Arg-PCN@Gel on the main polysaccharide intercellular adhesin (PIA) and eDNA were significantly strongest among the three nanosystems. Under irradiation for 30 min, the biomass of PIA was dropped to 37.33 \pm 13.60% (B1-1) and 13.67 \pm 3.86% (P1-2) when incubated with Arg-PCN@Gel (8 $\mu\text{g ml}^{-1}$), respectively (Fig. 5E and fig. S12), and their eDNA biomass was effectively decreased to 60.4 \pm 0.8 $\mu\text{g ml}^{-1}$ and 36.0 \pm 2 $\mu\text{g ml}^{-1}$, respectively (Fig. 5D). The best inhibition effect of Arg-PCN@Gel was because its surface gelatin was hydrolyzed by MRSA to provide more abundant NO under irradiation (Fig. 3, D and E) (28, 29). The ¹O₂ can more effectively down-regulate the *cidA* that regulates MRSA programmed death to restrain eDNA generation compared with NO and ONOO⁻ (Fig. 5F). Compared with ROS and ONOO⁻, the NO can more potently down-regulate the *icaA* encoding glucosamine *N*-deacetylase involved in PIA synthesis (Fig. 5G). These results suggest that Arg-PCN@Gel can effectively inhibit biofilm formation by down-regulating PIA and eDNA via the synergistic effects of different active substances of NO, ROS, and ONOO⁻.

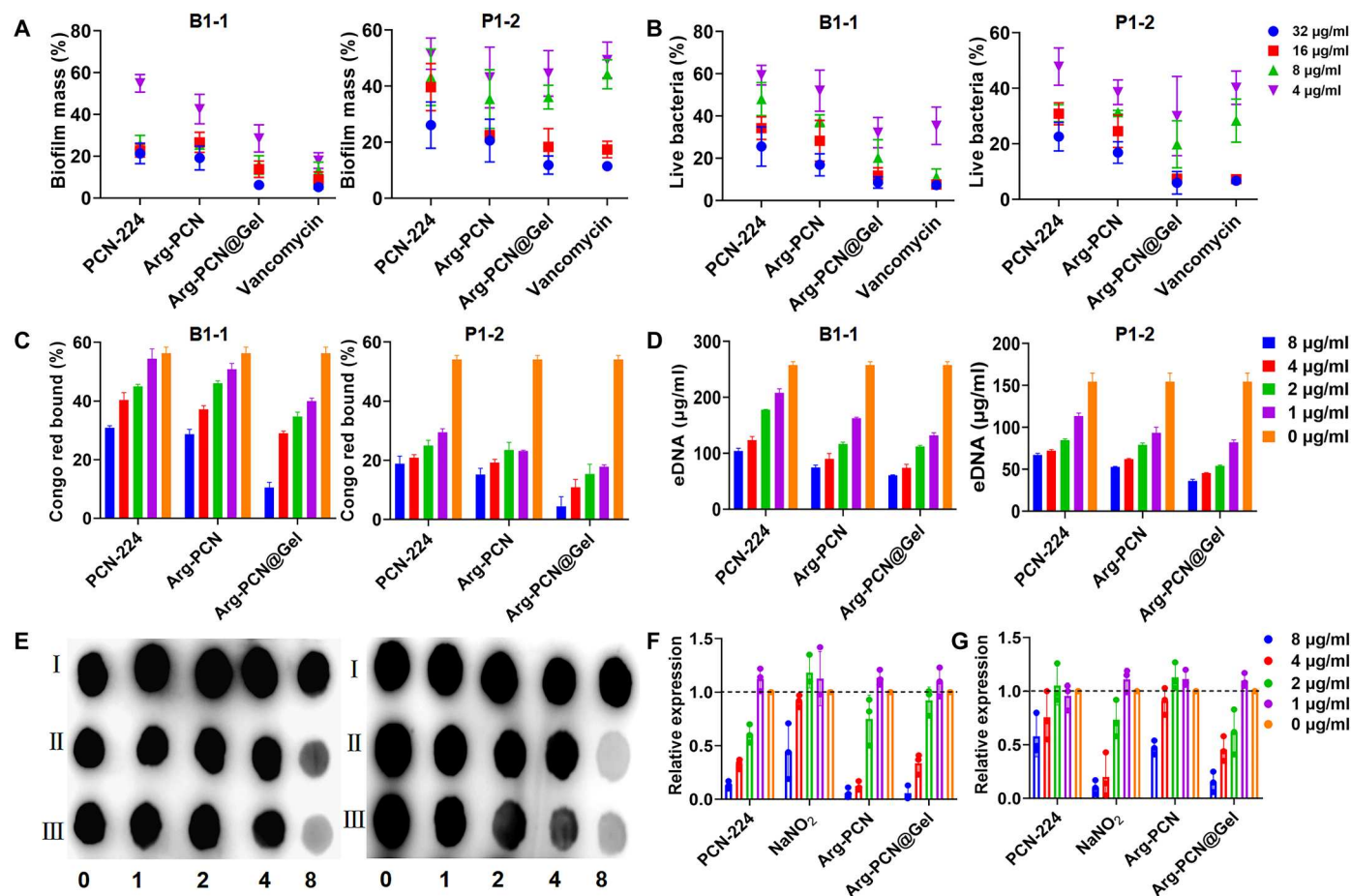


Fig. 5. Anti-biofilm formation of Arg-PCN@Gel. (A and B) Destructive of different treatments on biofilm-forming (A) and its internal bacteria (B). (C to E) Yields of exopolysaccharides (C), eDNA (D), and polysaccharide intercellular adhesin [(E), I: PCN-224, II: Arg-PCN, III: Arg-PCN@Gel, 0, 1, 2, 4 and 8: 0, 1, 2, 4 and 8 $\mu\text{g ml}^{-1}$]. (F and G) Expression level of *cidA* (F) and *icaA* (G).

Biofilm infections are difficult to cure due to their specific microbial community structure that inhibits the penetration of antimicrobial agents (4, 7). Therefore, it is very important whether the Arg-PCN@Gel can penetrate and thus eradicate the mature biofilms and its embedded MRSA with different metabolic states. After incubation for 1 hour, the fluorescence of Arg-PCN@Gel on biofilms was very higher compared to that of PCN-224 and Arg-PCN possibly due to the specific adhesion of gelatin to MRSA surface autolysin (Fig. 6A), despite its negative charge and higher hydrophilicity (41). The purplish-red fluorescence of Arg-PCN@Gel was gradually penetrated into the biofilms with prolonged incubation time and its penetration performance was more effective than the other two nanosystems (Fig. 6A). The three nanosystems exhibited dose-dependent activity against mature biofilms both in the dark and under irradiation, while the most efficient was Arg-PCN@Gel (Fig. 6, B and C, and figs. S13 and S14). Under irradiation, Arg-PCN@Gel ($4 \mu\text{g ml}^{-1}$) disrupted $42.10 \pm 3.38\%$ (P1-2) and $50.28 \pm 2.41\%$ (B1-1) biofilms, while it need Arg-PCN ($8 \mu\text{g ml}^{-1}$) and even up to vancomycin and PCN-224 ($16 \mu\text{g ml}^{-1}$) to produce equivalent destruction activity (Fig. 6B). When the concentration of Arg-PCN@Gel was increased to $32 \mu\text{g ml}^{-1}$, the live MRSA inside biofilms was reduced to $6.47 \pm 0.42\%$ (B1-1) and $8.49 \pm 2.05\%$ (P1-2) (Fig. 6C). Under further observation by confocal laser scanning microscopy, the anti-biofilm activity of PCN-224, Arg-PCN, and Arg-PCN@Gel was markedly increased after irradiation but not for vancomycin without penetration ability (Fig. 6D) (42, 43). The integrity impairment of mature biofilms was demonstrated by the enhanced susceptibility of lysostaphin against MRSA after treatment with nanosystems. Under irradiation for 30 min, the biofilm integrity damage degree order was the following: Arg-PCN@Gel and acid sodium nitrite (NaNO_2 ; equivalent to NO content produced by Arg-PCN@Gel) > Arg-PCN > PCN-224 (Fig. 6E). This indicates that the integrity was more effectively destroyed by NO compared with ROS and ONOO^- . Fortunately, Arg-PCN@Gel nearly completely eradicated the mature biofilms after irradiation and was more significantly effective than vancomycin.

The activity of Arg-PCN@Gel against MRSA embedded in mature biofilms was further studied by extracellular alkaline phosphatase (AKP) content and 2-nitrophenyl-beta-d-galactopyranoside (ONPG) hydrolysis test. The order of detected extracellular AKP concentration (an indicator of bacteria cell wall damage degree) was the following: Arg-PCN@Gel > Arg-PCN > PCN-224 > NaNO_2 (Fig. 6F), indicating that ONOO^- and ROS have stronger destruction against cell walls than NO. The cell membrane damage degrees treated by the different nanosystems at the same concentration were Arg-PCN@Gel, Arg-PCN, and PCN-224, while NaNO_2 hardly destroyed the cell membrane at 4 to $32 \mu\text{g ml}^{-1}$. These results suggested that the cell walls and membrane damage were mainly mediated by ROS and ONOO^- rather than NO (Fig. 6G). The result is consistent with a previous report that NO induces lipid peroxidation via triggering $^1\text{O}_2$ to produce ONOO^- to destroy the MRSA cell membrane (24). It can be speculated that the anti-biofilm effect of our designed Arg-PCN@Gel is via the layer-by-layer destruction from the biofilm surface to its internal bacterial cell membrane by synergistic effects of ROS, NO, and ONOO^- . In addition to the EPS barriers of biofilms, persistent bacteria inside biofilms are another important reason for the intractability of MRSA (44, 45). Therefore, the scavenging effects of bacterial colony variants inside biofilms by the nanosystems were

as follows: Arg-PCN@Gel > Arg-PCN > vancomycin > PCN-224 both in the dark and under irradiation (Fig. 6, H and I, and fig. S15). It can be concluded that Arg-PCN@Gel can effectively penetrate into the MRSA biofilms and generate different synergistic active substances under irradiation to effectively remove biofilms and their internal active and persistent MRSA.

Targeting therapy of MRSA biofilm-associated infections

In view of the excellent anti-biofilm and inactivated biofilm-embedded MRSA performances of our designed Arg-PCN@Gel in vitro, its targeting therapy performances were systematically evaluated in the mouse subcutaneous MRSA biofilms infection model (fig. S16) (46). The peak fluorescence intensity at the infected sites was reached 1 day after intravenous injection, and then gradually declined with time (Fig. 7, A and B). Although the three nanosystems all reached the peak concentration at the infection site 1 day after administration, the fluorescence intensity of Arg-PCN@Gel at the infection site was 3.36 and 8.39 times higher than that of Arg-PCN and PCN-224, respectively. Furthermore, the retention capacity of Arg-PCN@Gel (15 days) at the infected site was much longer than PCN-224 (7 days) and Arg-PCN (11 days) (Fig. 7, A and B). The fluorescence intensity of Arg-PCN@Gel after 1 day of administration was very low except in the liver, while a large amount of PCN-224 and Arg-PCN appeared in the liver, spleen, and lung (Fig. 7, C and D). The specific distribution of nanosystems in the lung may be due to the ligand TCPP, which can strongly bind to low-density lipoprotein and CD_{320} receptors on lung cancer cells to promote their uptake by lung cancer cells (47). Fluorescence intensity of Arg-PCN@Gel in different organs except the liver was lower than that of PCN-224 and Arg-PCN after 15 days of administration (Fig. 7C). The targeting delivery and retention capacity of Arg-PCN@Gel at the infected site might be due to its charge transformation from positive to a negative value (Fig. 2D), enhanced hydrophilicity (Fig. 2G) to avoid phagocytosis of the mononuclear reticular cell system, and active targeting to MRSA mediated by *atl* (Fig. 4G) (27–29, 48).

Because of the target retention of Arg-PCN@Gel at the MRSA infection site for 15 days, the anti-biofilm treatment scheme was administered by a single dose and irradiated by red light once a day (Fig. 7E). Although the injection dosage of Arg-PCN@Gel was 4.5-fold lower than the vancomycin dose, the Arg-PCN@Gel was more significantly effective against biofilm infections (Fig. 7, F and G). The vancomycin-treated group only showed a better therapeutic effect within the first 2 days, while the Arg-PCN@Gel exhibited a more significantly anti-biofilm effect than vancomycin after 3 to 10 days of administration via abscess healing values. The lower effects within the first 2 days might be that the high dose of vancomycin has a direct effect after intravenous administration, while Arg-PCN@Gel needs to generate active substances under irradiation to fight against infections. As shown in Fig. 7G, the biofilms were still detected at the infected sites in the other treatment groups after 7 days of treatment, except for the Arg-PCN@Gel irradiation treatment group. In addition, the Arg-PCN@Gel irradiation group [$4.8 \pm 0.27 \log_{10}$ [colony-forming units (CFU) g^{-1}]] showed a more effective decrease in MRSA number compared with the vancomycin group [$6.25 \pm 0.97 \log_{10}$ (CFU g^{-1})] and the saline group [$9.32 \pm 0.12 \log_{10}$ (CFU g^{-1})] (Fig. 7, H and J). At the end of the experiment, the colony count of the Arg-PCN@Gel irradiation group was still lower than that of the vancomycin group. In the

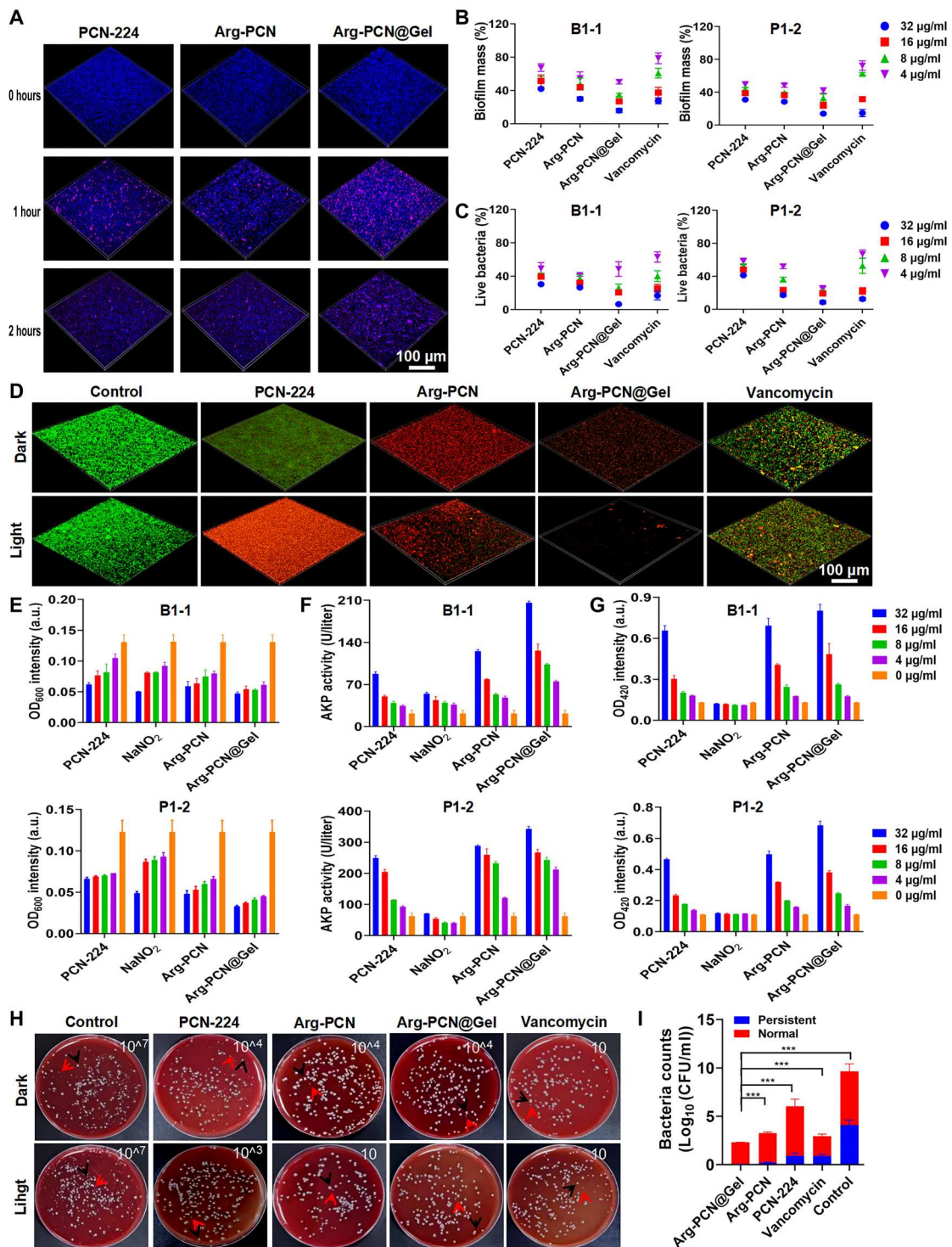


Fig. 6. Anti-biofilm activity. (A) Penetration and accumulation of nanosystems on biofilm. (B and C) Destructive of different treatments on biofilm (B) and its internal bacteria (C). (D) Living and dead biofilms treated with different nanosystems and vancomycin. (E to G) The sensitivity to lysostaphin (E), alkaline phosphatase activity (F), and ONPG hydrolysis activity (G) of B1-1 and P1-2 treated with different nanosystems and vancomycin, respectively. (H and I) Representative plate (figures in each image represent dilution ratio) (H) and plate counts (I) of persistent and normal bacteria inside biofilms. OD₆₀₀, optical density at 600 nm.

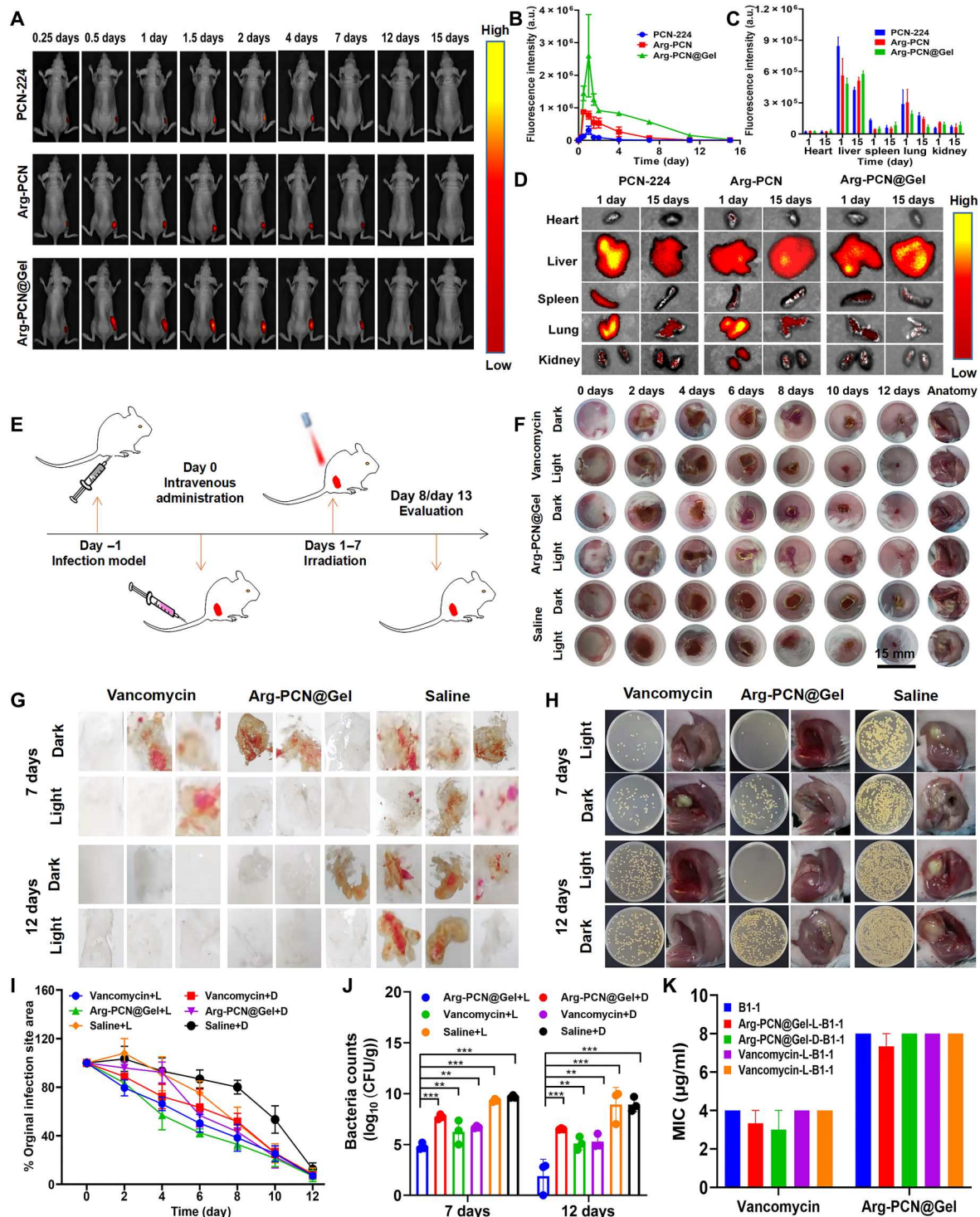


Fig. 7. Targeted therapy. (A and B) Fluorescence images (A) and intensity-time curves (B) of the infection site. (C and D) Fluorescence images (C) and intensities (D) of organs. (E) Targeted therapy procedure. (F and G) Representative images (F) and biofilms (G) of the infected site. (H and I) Representative images (H) and size-time curve (I) of the infected site after different treatments. (J) Colony count at infection sites. (K) Sensitivity of isolates to vancomycin and Arg-PCN@Gel.

saline group, it was found that there was still pus and biofilm in the muscle tissue at the infected site, which lead to more serious persistent infection (Fig. 7, H and I).

Antibiotic resistance induced by long-term usage of antibiotics is a serious global problem. Therefore, the sensitivity of MRSA isolated from the site of infections after treatment of Arg-PCN@Gel was tested. The strains isolated from the Arg-PCN@Gel irradiation group were equal or slightly more sensitive to MRSA before treatment and isolated from the vancomycin treatment group (Fig. 7K). This may be due to Arg-PCN@Gel damaging the cell wall and membrane structure of MRSA via multimodal mechanisms ($^1\text{O}_2$, NO, and ONOO $^-$) after irradiation (Fig. 6, E to G) (49, 50). The Arg-PCN@Gel shows great potential in the treatment of MRSA biofilm-associated infections without resistance.

Arg-driven nutritional immunotherapy effects in vitro and in vivo

Because of biofilm resistance to the host immune system, the inflammation at the infection site is persisted and is difficult to heal (4, 5). Arg, as an important nutrient medium in the immune response, can participate in the initial inflammation and the subsequent regression of inflammation (21). Initially, infected tissue secretes a large amount of pro-inflammatory factors (such as TNF- α , interferon- γ , IL-1), and M1-like macrophages at the infected site can consume Arg to produce NO through a high expression of iNOS to fight infection (20–21, 51). At the same time, NO itself can further induce the expression of iNOS to use Arg. Once NO is excessive, it will promote transformation from the pro-inflammatory stage to the anti-inflammatory stage, and thus, the host turns to secrete amounts of anti-inflammatory factors (e.g., IL-4, IL-10, IL-13, and transforming growth factor- β). The M2-like macrophages are prompted to convert Arg into polyamines via Arg-1 to promote tissue repair (52). Therefore, the efficiency of Arg-driven nutritional immunotherapy of our designed nanosystems was evaluated in vitro and in vivo.

In vitro results showed that PCN-224, Arg-PCN, and Arg-PCN@Gel hardly lead normal RAW264.7 cells to overexpress the pro-inflammatory factors (iNOS and TNF- α) and anti-inflammatory factors (Arg-1 and IL-4) in the dark (fig. S17), suggesting that Arg itself does not influence the cellular immunity without PDT and inflammation. After irradiation, the enhanced pro-inflammatory factors and Arg-1 of normal cells incubated with Arg-PCN and Arg-PCN@Gel were similar to those of cells treated with NaNO $_2$ (figs. S17 and S18), indicating NO produced by Arg and $^1\text{O}_2$ under irradiation can effectively trigger an immune response. Although PCN-224 slightly elevated immune levels, the host cell is relatively sensitive to ROS compared to bacteria, which easily results in cytotoxicity. In the dark, the expression level order of immune factors of infected cells was as follows: NaNO $_2$ > Arg-PCN@Gel > Arg-PCN > Arg > PCN-224 > control (Fig. 8A). Under irradiation for 6 hours, the concentration of pro-inflammatory produced by infected cells incubated with Arg-PCN and Arg-PCN@Gel was significantly higher than those of PCN-224, Arg, and control, while the anti-inflammatory factors were only slightly higher. For 24 hours, the concentration of the anti-inflammatory factors was significantly higher, while the pro-inflammatory factors incubated with Arg-PCN and Arg-PCN@Gel were significantly lower than those of PCN-224, Arg, and control. These results indicate that the two nanosystems contribute to

transforming from the pro-inflammatory stage to the anti-inflammatory stage of infected cells to repair cell damage. It has been reported that NO has a biphasic effect on immune factors, promoting the expression of iNOS at low concentrations to produce more NO for antibacterial effects, and promoting the production of anti-inflammatory factors at high concentrations to prevent excessive NO from promoting cell repair (21, 53–54). As reported, irradiation-promoted Arg-PCN@Gel and Arg-PCN produce NO, which induced iNOS expression and further used Arg to produce NO. Therefore, after 6 hours, the concentration of NO in the Arg-PCN@Gel, Arg-PCN, and NaNO $_2$ treatment groups was significantly increased, reducing the bacterial count of infected cells (figs. S19 and S20). A high concentration of NO can not only resist infection but also activate anti-inflammatory factors to inhibit the production of NO to repair damaged cells. After 24-hour treatment, NO concentration and bacterial counts in Arg-PCN@Gel and Arg-PCN were significantly decreased, while the anti-inflammatory factors Arg-1 and IL-4 were increased significantly (Fig. 8A and figs. S19 and S20). Arg-PCN@Gel can provide more Arg and thus result in higher anti-inflammatory factors at the late stage of infections compared with Arg-PCN.

To further evaluate the immunotherapeutic effect, the expression of immune factors at the infection site of mice was detected at different time points after treatment. On the first day of treatment, the anti-inflammatory factor level of the vancomycin-treated group was slightly higher than that of the Arg-PCN@Gel group due to the directed anti-biofilm effect of high-dose vancomycin and the inability of Arg-PCN@Gel to provide NO without PDT (Fig. 8, C and D). After irradiation, the pro-inflammatory factor (TNF- α , IL-1 β , and IL-6) expression levels in the Arg-PCN@Gel groups before 3 days were similar or slightly lower comparable to the vancomycin group, but iNOS expression levels of Arg-PCN@Gel was higher than vancomycin (Fig. 8, B and D, and fig. S19). The high expression of iNOS will contribute to the use of Arg to promote an immune response against infection. On the 7th and 12th day of treatment, the pro-inflammatory factors of the Arg-PCN@Gel irradiation group were lower than those of the vancomycin-treated and normal saline groups, while the anti-inflammatory factors of IL-4 and Arg-1 were higher than those of the vancomycin-treated and normal saline groups, indicating that Arg might be converted into polyamines via high expression Arg-1 to promote tissue repair (55). Because of the enhanced immunotherapy effects by Arg via iNOS/NO axis and arginase/polyamine axis as well as efficient target PDT, the abscess therapy effect in the Arg-PCN@Gel irradiation group was more excellent and basically cured. Thus, the level of pro-inflammatory and anti-inflammatory factors in the Arg-PCN@Gel irradiation group was significantly lower compared to the vancomycin-treated and normal saline groups on the 12th day (Fig. 8, B to D, and fig. S21).

The expression of Arg-1 and iNOS is related to the polarization profile of macrophages. On the third and seventh day of treatment, CD $_{86}$ (a marker for M1-like macrophages) and CD $_{206}$ (a marker for M2-like macrophages) in the vancomycin group were at a high expression level (Fig. 8E and fig. S22) (52). As we expected, the CD $_{86}$ in the Arg-PCN@Gel group was significantly decreased, while the CD $_{206}$ was maintained at a high level, which is conducive to the recovery of infected tissues. After 12 days of treatment, the CD $_{206}$ in the Arg-PCN@Gel irradiation group was also decreased, which was consistent with expression levels of Arg-1, iNOS, and other immune

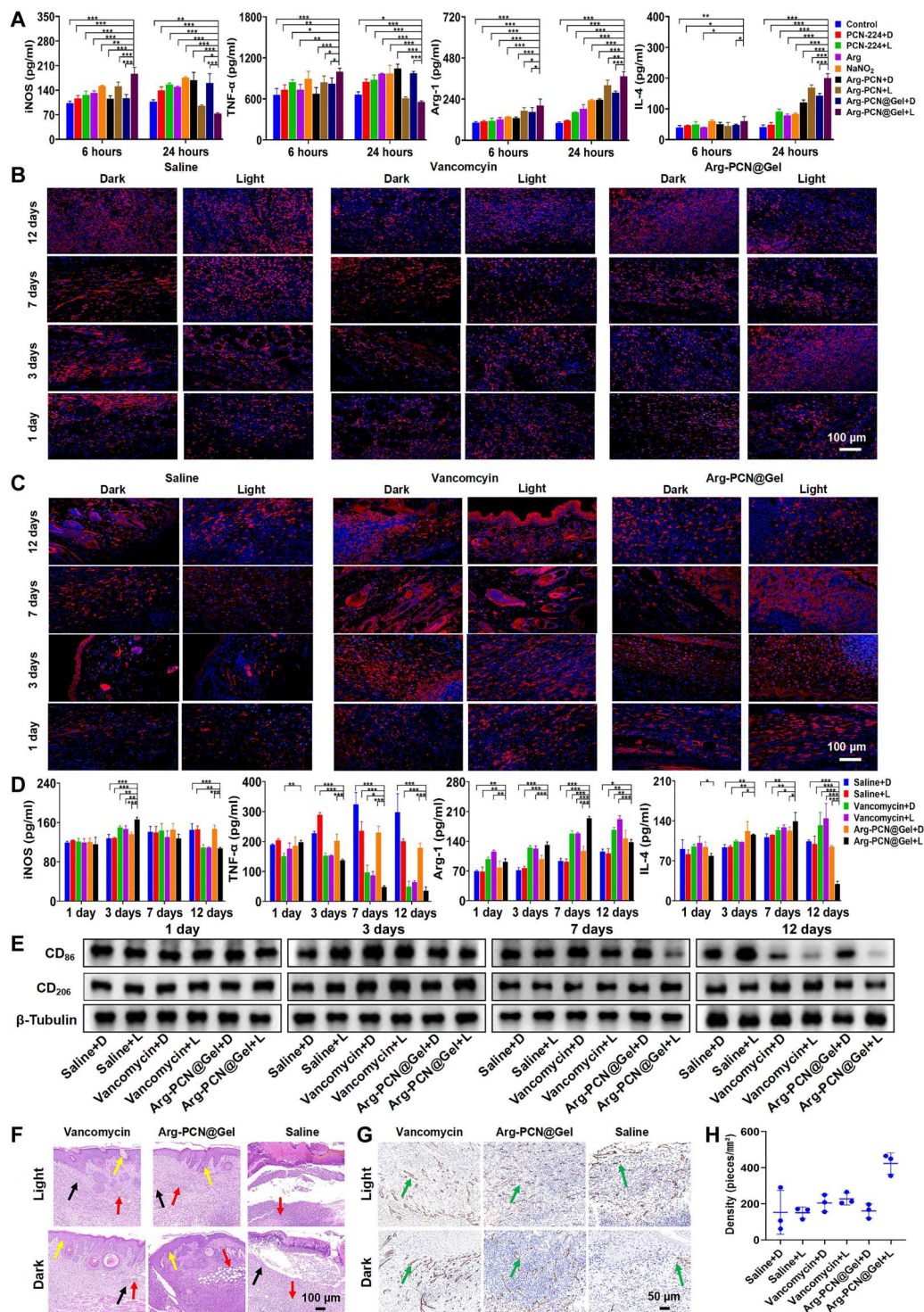


Fig. 8. Nutritional immunotherapy. (A) Arg-1, IL-4, iNOS, and TNF- α were expressed in infected cells after different treatments. (B and C) Immunological fluorescence sections of iNOS (B) and Arg-1(C) at the infected site. (D) Expression of Arg-1, IL-4, iNOS, and TNF- α at the infected site. (E) Expression of CD₈₆ and CD₂₀₆ at the infected site on different days after treatments. (F) Representative hematoxylin and eosin images (black arrows: blood vessels; yellow arrows: spinous layers; red arrows: inflammatory cells). (G and H) Representative images (G) (green arrows: CD₃₁-positive cells) and number (H) of CD₃₁-positive cells.

factors. The histomorphology and immunology analysis of infected sites also showed satisfactory therapy effects (Fig. 8, F to H) on the 12th day. Compared with the accumulation of necrotic cells and infiltration of neutrophils in the skin of the vancomycin-treated group, the Arg-PCN@Gel irradiation group not only more markedly reduced the infiltration of inflammatory cells but also showed more abundant new vessels (Fig. 8, F and G). The CD₃₁-positive cells in the Arg-PCN@Gel irradiation group even reached up to 423.13 ± 48.56 pieces mm^{-2} (Fig. 8H). All these results indicate that the Arg-PCN@Gel irradiation group more potent therapy effect.

Molecular mechanism of Arg-PCN@gel against biofilms

The anti-biofilm molecular mechanism of Arg-PCN@Gel was examined by transcriptomics. The Arg-PCN@Gel had a great impact on the transcription of MRSA, including the down-regulated expression of 417 genes and the up-regulated expression of 297 genes (figs. S23 and S24). These genes were involved in 99 pathways analyzed by the Kyoto Encyclopedia of Genes and Genomes (KEGG) enrichment analysis, among which 20 pathways with the most significant enrichment are shown in fig. S25. To verify the RNA-sequencing results, nine genes associated with biofilms were selected to confirm their expression level (fig. S26). The expression of all selected genes was consistent with the trend of RNA sequencing (RNA-seq) results, indicating that RNA-seq can validate the analysis of genetic evidence from transcription.

It is expected that *atl*, which can contribute Arg-PCN@Gel to adhere MSRA, was up-regulated (figs. S24 and S26). In addition, gelatin can promote the internalization of Arg-PCN@Gel by MRSA (56). As incubation time increased, the nanosystems more effectively adhered to the bacterial surface and even enter into MSRA (Figs. 4G and 9, A to C) confirmed by flow cytometry and TEM. The intact Arg-PCN@Gel (red arrow in the figure) can be seen inside MRSA (Fig. 9C). The adhesion and intracellular distribution of Arg-PCN@Gel will adequately play the antibacterial and anti-biofilm effects via their produced ROS, NO, and ONOO⁻ due to the shortened distance between active substances (especially ¹O₂) and bacteria (41, 57). After irradiation, these active substances produced by Arg-PCN@Gel significantly affected the bacterial "two-component system," "pentose phosphorylation pathway," "pyrimidine metabolism," "glycolysis," and "pyruvate metabolism," which might be related with bacterial metabolic disorders with the unbalanced distribution of elements [e.g., O, copper (Cu), sulfur (S), and arsenic (As)] (Fig. 9, D and E, and fig. S25). Simultaneously, the up-regulated repressor regulating gene *arsR* also contributed to the decrease of bacterial As, and the down-regulated metal chaperone *copZ* could help to decrease Cu homeostasis system of MSRA (fig. S24) (55, 58). This may be due to the attack of ROS, NO, and ONOO⁻ on iron-sulfur cluster proteins and copper binding cytoplasmic proteins in the tricarboxylic acid cycle enzymes, reducing adenosine 5'-triphosphate (ATP) production (Fig. 9F), and the transient depletion of NADH, resulting in oxidative damage to cells (59–61). The arsenate reductase in MRSA, as a detoxification system, only has enzymatic activity when coupled with thioredoxin, thioredoxin reductase, and a reduced form of nicotinamide adenine dinucleotide phosphate. It is easily inactivated by oxidative stress to induce As unbalance (55, 62).

Besides, Arg-PCN@Gel down-regulated the carbon catabolite protein A (*ccpA*) to limit energy using efficiency (figs. S24 and

S26), which controls the carbon and nitrogen catabolites (63). In addition to *ccpA*, down-regulated *codY* (another global transcription factor) could also decrease the levels of guanosine triphosphate and isoleucine in MRSA (figs. S24 and S26) (64). It is reported that *codY* and *ccpA* jointly sense the nutritional and control carbon and nitrogen fluxes by controlling catabolism and anabolism involved in sugar and amino acid utilization (63, 64). Therefore, the metabolic activity of MRSA after different treatments was tested. The results showed that these nanosystems inhibited the metabolic activity of MRSA after irradiation, especially Arg-PCN@Gel (Fig. 9G). The down-regulation of *codY* and *ccpA* will decrease MSRA glycolysis and pyruvate metabolism (Fig. 9I). Both *ccpA* and *codY* could inhibit the Arg metabolism genes (*arcA*, *arcB*, *arcC*, and *arcD*) necessary for the survival of MRSA inside biofilms and proline auxotrophy (Fig. 9I and fig. S24). The *arcD* of MRSA is responsible to compete with the host to ingest Arg to meet its own energy needs and delay the host cell anti-inflammatory process to achieve chronic infection (21). As reported, the nanosystems significantly inhibited ATP in MRSA after irradiation, with the following inhibition efficiency order: Arg-PCN@Gel > Arg-PCN = NaNO₂ > PCN-224, indicating that the inhibitory effect of nanosystems on the ATP of MRSA mainly depends on NO (Fig. 9F). The decrease of *arcD* will contribute to Arg usage by host to produce immunological reaction (21, 22). Moreover, the decline of *ccpA* can reduce MRSA replication and PIA formation (53).

The *codY*, as the upstream main regulator of global regulators of MRSA, can control the two-component system *saeRS* and *srrB* (65, 66). The global regulator *ccpA* can use fatty acid kinase to activate *saeRS*. The *saeRS* can positively regulate the expression of the adhesion gene, lipase, and extra protein of MRSA (67). Thus, the down-regulation of *saeRS* may be related to the decrease of *sdrD*, a member of the MSSRAMM family adhesin (Fig. 9I and fig. S24). The down-regulation of *saeRS* inhibited the lipase activity of MRSA, and the inhibition rate of lipase activity in the Arg-PCN@Gel, Arg-PCN, PCN-224 irradiation treatment group, and NaNO₂ was $45.65 \pm 1.37\%$, $28.85 \pm 2.31\%$, $21.10 \pm 4.38\%$, and $8.17 \pm 2.20\%$, respectively (Fig. 9H). The results also showed that ROS and ONOO⁻ had a stronger inhibitory effect on MRSA lipase compared to NO. Simultaneously, the down-regulated *srrB* can up-regulate *tar* and *atl* and thus reduce DNA and protein release from reducing biofilm formation (68). In addition, up-regulated *isaA* and down-regulated *fstL* can also contribute to reducing DNA and protein formation to prevent biofilms (Fig. 9I and fig. S24).

In this study, a targeting and arginine-driven synergizing cascading PDT with nutritional immunotherapy nanosystems (Arg-PCN@Gel) for combating MRSA biofilms was neatly designed: the nanosystems containing core PCN-224 as a PDT platform for providing ROS, incorporating arginine as nitric oxide (NO) donor to cascade with ¹O₂ to produce more lethal ONOO⁻ and promote immune response, and coating with gelatin as a targeting agent and a persistent arginine provider. Its preparation and characterization, cascading products of different active substances capacity-triggered by red light, prophylaxis and eradication effects against biofilms and its embedded MRSA by different active substances, targeting therapy of MRSA biofilm-associated infections, and synergizing PDT effects with Arg-driven nutritional immunotherapy were systematically studied. The detailed molecular mechanism of Arg-PCN@Gel against biofilms was further investigated

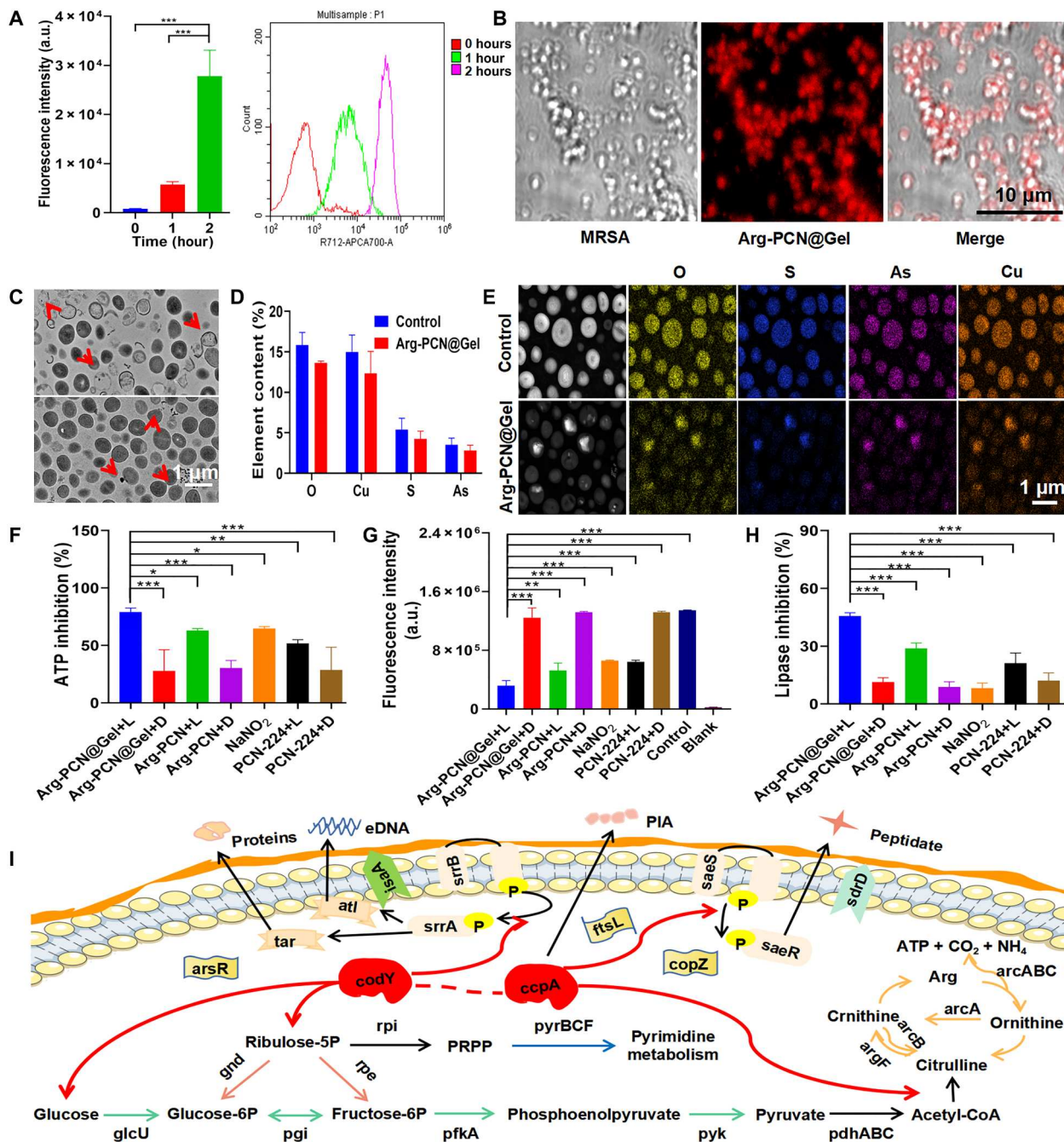


Fig. 9. Anti-biofilm mechanism of Arg-PCN@Gel. (A and B) Bacteria uptake to Arg-PCN@Gel after incubation within 2 hours. (C to E) Cellular structure (C), quantitative (D), and qualitative elemental analysis (E) of Arg-PCN@Gel-treated MRSA. (F to H) ATP (F), metabolic activity (G), and lipase (H) inhibition of MRSA after different treatments. (I) Anti-biofilm mechanism of Arg-PCN@Gel.

via transcriptomics. To verify the molecular mechanism, the metabolic activity, ATP content, and lipase activity of MRSA were determined after treatment with Arg-PCN@Gel. The excellent prophylaxis and targeting therapy effects against biofilms and the embedded MRSA suggest that our designed Arg-PCN@Gel might be an important candidate for innovative antibacterial agents to treat intractable MRSA biofilm-associated infections. The anti-biofilm mechanism of each active species and their synergistic

effects with Arg nutritional immunity elucidated in this study may contribute to the further development of PDT. The dynamic regulation between the pro-inflammatory and anti-inflammatory stages of the Arg nutritional immune response was elucidated in vitro by changes in NO concentration, further elucidation in vivo of this issue remains challenging.

MATERIALS AND METHODS

Materials

TCPP (purity: >97%) was purchased from Ark Pharm (Chicago, IL, USA). $ZrOCl_2 \cdot 8H_2O$ was obtained from Sigma-Aldrich (St. Louis, MO, USA). Gelatin (purity: >99%) was bought from Tianjin Guangfu Institute of Fine Chemicals (Tianjin, China). ATP luminescent was purchased from Yeasen Biotechnology Co., Ltd. (Shanghai, China). A nitric oxide content detection kit and resazurin were purchased from Solarbio Life Science (Beijing, China). The reactive oxygen detection kit was bought from Beyotime Institute of Biotechnology (Jiangsu, China). Lysozyme, FastPure Cell/Tissue Total RNA Isolation Kit V2, HiScript IIQ RT Super Mix for quantitative polymerase chain reaction (qPCR) (+gDNA wiper), and ChamQ Universal SYBR qPCR Master Mix were obtained from Vazyme Biotech Co., Ltd. (Nanjing, China). Vancomycin was acquired from Hubei Weideli Chemical Technology Co., Ltd. (Wuhan, China). Horseradish peroxidase-labeled wheat germ agglutinin was obtained from Alpha Diagnostic Intl. Inc. (TX, USA). Ruthenium red, sodium deoxycholate, disodium *p*-nitrophenyl phosphate hexahydrate, and purple crystal were acquired from Shanghai Yuanye Biotechnology Co., Ltd. (Shanghai, China). RNA extraction kits were purchased from Qiagen (Dusseldorf, Germany). PCR-02-C was bought from Axygen (Silicon Valley, CA, USA). EU 8-tube strips were purchased from GeneBrick (NC, USA). SOSG and FilmTracer LIVE/DEAD biofilms Viability Kit were bought from Thermo Fisher Scientific (MA, USA). Ciprofloxacin and cefoxitin were acquired from China Institute for Food and Drug Control (Beijing, China). Tris-buffered saline, nitrocellulose membrane, and 4',6-diamidino-2-phenylindole (DAPI) were bought from Biosharp (Anhui, China). Bovine serum albumin, proteinase K, and Arg were purchased from BioFroxx (Einhausen, Germany). Trypticase soy broth (TSB), LB, LB nutrient agar, and brain heart infusion agar medium were bought from Haibo Biotechnology (Qingdao, China). LDH and AKP kits were purchased from Nanjing Jiancheng Bioengineering Institute (Nanjing, China). Naphthalene ethylenediamine hydrochloride, ONPG, Congo red, and gentamicin were bought from Macklin (Shanghai, China). Benzoic acid, anhydrous calcium chloride ($CaCl_2$), *p*-aminobenzenesulfonic acid, $NaNO_2$, SDS, phenol, chloroform, isoamyl alcohol, sodium acetate, anhydrous ethanol, Tween 20, EDTA, methanol, glacial acetic acid, and sucrose were bought from Sino-pharm Chemical Reagent Co., Ltd. (Shanghai, China). Mouse TNF- α , IL-1 β , IL-6, IL-4, and IL-10 enzyme-linked immunosorbent assay (ELISA) kits were acquired from Hangzhou Lianke Biotechnology Co., Ltd. (Hangzhou, China).

Preparation of Arg-PCN@gel

Fifty milligrams of TCPP, 1.4 g of benzoic acid, and 150 mg of $ZrOCl_2 \cdot 8H_2O$ were added into a round-bottomed flask containing 50 ml of *N,N'*-dimethylformamid, sonicated for 1 min, and reacted at 90°C for 4 hours. PCN-224 was collected by centrifugation and sequentially washed to remove unreacted reaction precursor and solvent. Last, PCN-224 was dried at 105°C overnight. PCN-224 and Arg were simultaneously resuspended in 50% ethanol solution at a ratio of 1:1, and then reacted to obtain Arg-PCN at 40°C for 24 hours. The 50-mg Arg-PCN was resuspended in 100 ml of 2% gelatin solution, and, subsequently, 1 M $CaCl_2$ (3 ml) was added as a cross-linking agent to acquire Arg-PCN@gel at 40°C for 1 day.

Characterization of Arg-PCN@gel

The particle size, polydispersity index, and ZP of PCN-224, Arg-PCN, and Arg-PCN@gel were measured by Zetasizer ZX3600 (Malvern Instruments, UK). The morphologies of three nanosystems were observed by Hitachi X-650 (Hitachi Ltd., Japan). The UV absorption wavelengths of nanosystems and individual components were determined by a UV-Vis spectrophotometer (PerkinElmer Ltd., MA, USA). Their chemical structure and interaction among different components were studied by infrared spectroscopy (Bruker, Germany). The crystal form of nanosystems was determined by x-ray diffractometer (Bruker, Germany) at a scanning interval of 3° to 50°, scan rate of 5° min⁻¹, step size of 0.02°, and scan at a small angle. Their hydrophilicity and hydrophobicity were determined by DSA25-immobilized drop contact angle (Bruker, Germany).

Determination of ROS and ¹O₂

The 10 μ l of 5 μ M SOSG fluorescent probe methanol solution or a 10 μ M DCFH-DA probe was added into 5 μ l of PCN-224, Arg-PCN, and Arg-PCN@gel suspension, and then evenly mixed with 85 μ l of water. Under irradiation with laser (660 nm) for different time points, the fluorescence intensity was measured by a multilabel microplate detection system (PerkinElmer Ltd., MA, USA) at excitation/emission (Ex/Em) of 490/520 (SOSG) and 488/525 (DCFH-DA). After incubation for 20 min with a 10 μ M DCFH-DA probe in attached RAW264.7 cells, the free probe was washed off and the culture medium containing different nanosystems (4 μ g ml⁻¹) was added. After 30 min of irradiation, the culture medium was washed off, DAPI was added and incubated at 37°C for 25 min, and the production of ROS on the cells was observed by fluorescence microscope.

Enzyme responsiveness

Arg release of Arg-PCN@gel when adding MMPs was determined by high-performance liquid chromatography. After the addition of 1 mg of Arg-PCN@gel into MMP solution (0.1 mg ml⁻¹) kept at 37°C, the sampling was collected at different times to detect the released Arg, respectively. Simultaneously, the *S. aureus* group (MMP-positive, 10⁸ CFU ml⁸) was set as the positive control and the *E. coli* group (MMP-negative, 10⁸ CFU ml⁸) and Arg-PCN@gel without MMPs enzyme were set as the negative controls.

Detection of NO

The release of NO was detected by the Griess reagent. Different concentrations of $NaNO_2$ solutions were reacted with the Griess reagent. After the reaction for 20 min, the solution absorbance (OD₅₄₀, optical density at 540 nm) was detected by a UQuant microplate reader (BioTek Instruments, Inc., VT, USA). The three nanosystems and their respective mixtures with MMP were irradiated by laser for 30 min. The supernatant of the reaction systems was reacted with Griess reagent, and, subsequently, the absorbance of generated NO was quantitatively measured by UQuant microplate reader.

Detection of ONOO⁻

Twenty micromolar L-tyrosine was respectively mixed with different nanosystems and $NaNO_2$ (200 μ g ml⁻¹) in equal volume, and then irradiated for 30 min (69). Subsequently, the ONOO⁻ amount was detected by an RF6000 fluorescence spectrophotometer (Shimadzu, Japan) at Ex/Em of 200/465 nm.

Hemolysis

A total of 0.9 ml of 2% red blood cell suspension was mixed with 0.1 ml of saline containing different concentrations (calculated by TCPP concentration) of nanosystems. After culturing at 37°C for 2 hours, the absorbance (OD₅₄₀) of the supernatant was detected by a UQuant microplate reader to calculate the hemolysis rate. Simultaneously, saline and Triton X-100 were set as negative and positive controls, respectively.

$$\text{Hemolysis rate(\%)} = \frac{(\text{sample OD value} - \text{negative control OD value})}{(\text{positive control OD value} - \text{negative control OD value})} \times 100\%.$$

Cytotoxicity

The NIH/3T3 cells were added into a 96-well plate containing 10⁴ cells per well and incubated at 37°C in a 5% CO₂ incubator for 24 hours. After complete adherent, the old medium was replaced by 200 μl of fresh medium with different concentrations of the three nanosystems. After coinubation for 2 hours, the 96-well plate was irradiated for 0, 10, 20, and 30 min, respectively. When continuing the culture for 24 hours, the NIH/3T3 cell morphology was observed with a microscope. Cell viability and LDH activity were further determined by 3-(4,5-dimethylthiazol-2-yl)-2,5-diphenyltetrazolium bromide (MTT) (5 mg ml⁻¹) and an LDH detection kit. The OD₅₇₀ and OD₄₅₀ were determined by a UQuant microplate reader after adding 20 μl of MTT solution and LDH kit treatment, respectively. The calculation formulas are as follows

$$\text{Cell viability (\%)} = \frac{(\text{sample OD value}/\text{control OD value})}{\times 100\%}.$$

$$\text{LDH activity(\%)} = \frac{(\text{sample OD value}/\text{control OD value})}{\times 100\%}.$$

Antibacterial activity

Two clinical isolates of MRSA (10⁶ CFU ml⁻¹) (B1-1 and P102, preserved in the National Veterinary Drug Residues Reference Laboratory of Huazhong Agricultural University) at logarithmic growth stage were coinubated with PCN-224, Arg-PCN, and Arg-PCN@Gel for 30 min, the adhesion of nanosystems to MRSA was observed by TEM. The MICs of the three nanosystems were determined by the micro broth double dilution method. Briefly, the bacterial diluent (2 × 10⁶ CFU ml⁻¹) and the culture medium containing nanosystems with different concentrations are added into 96-well plates in equal volume. The negative control wells were cultured without nanosystems and MRSA, and the positive control only contained bacteria. The groups were irradiated for 0, 10, 20, and 30 min, respectively, and then placed into a 37°C incubator for 18 to 24 hours at a speed of 200 rpm.

The MRSA treated with different nanosystems of 8 μg ml⁻¹ under irradiation and dark were collected by centrifugation. The bacteria precipitation was washed with phosphate-buffered saline (PBS), and then redispersed and fixed with glutaraldehyde (4% w/w) for 4 hours. The precipitation was dehydrated in a gradient of 20 to 100% (v/v) ethanol solution (15 min each time). The treated MRSA morphology was observed by SEM after freeze-drying and

sprayed gold. After MIC determination, the bacteria solution without obvious bacteria growth was properly diluted, and then, 100 μl of bacteria solution was poured into agar plates to detect MBC. The colony in agar plates was counted after culturing for 24 hours. The bactericidal kinetics of the three nanosystems were determined under MBC concentration. After the nanosystems were added and then irradiated for 30 min, samples were collected at the fixed times and subsequently diluted 10ⁿ (n = 0, 1, 2, 3.....) to inoculate on agar plates for bacterial counts. In addition, the bacteria solution in the MBC wells of Arg-PCN@Gel was collected and washed with PBS. Glutaraldehyde (4% w/w) was added and fixed for 4 hours, and then prepared into sections for TEM observation and energy-dispersive spectroscopy analysis.

Biofilms formation

The 200 μl of logarithmic growth period MRSA solution (10⁸ CFU ml⁻¹) was added into 96-well plates, and then cultured at 37°C incubator for 24 hours to obtain mature biofilms.

Crystal violet staining and MTT

The different concentrations of three nanosystems and vancomycin were added into the mature biofilms, and then incubated for 2 hours. The treatment of the biofilm-forming ability test is as follows: the diluted MRSA solution (10⁹ CFU ml⁻¹) of 180 μl was added into a 96-well plate, and then 20 μl of different nanosystems was added to incubate for 2 hours. Subsequently, it was incubated for 24 hours after being irradiated for 30 min. The anti-biofilm activity of the nanosystems was detected by crystal violet staining and MTT (70). The dark groups were detected as the same method without 30-min irradiation.

Formation of extracellular polysaccharide

MSRA (2 × 10⁸ CFU ml⁻¹) was respectively cocultured with equal volumes of PCN-224, Arg-PCN, and Arg-PCN@Gel with different concentrations for 24 hours, and TSB as a control. The biofilms were washed and resuspended with 1 ml of saline. Congo red was added to the above solution to ensure that its concentration was 40 μg ml⁻¹. Subsequently, it was incubated in a constant temperature shaking table at 37°C and 200 rpm for 2 hours. The absorbance of the supernatant was measured at 490 nm. For detection, 1 ml of Congo red-containing saline solution was used as a control. The calculation formula for the Congo red binding rate is as follows

$$\text{Congo red binding rate(\%)} = 100 - \left[\frac{(\text{test supernatant OD} \times 100)}{\text{control group OD}} \right].$$

Determination of PIA and eDNA formation ability

The same volume of bacteria solution (10⁸ CFU ml⁻¹) and different concentrations of PCN-224, Arg-PCN, and Arg-PCN@Gel were added to a 12-well plate. After incubation for 2 hours, it was treated with and without irradiation for 30 min. Subsequently, they were cultured in a 37°C constant temperature oscillation incubator for 24 hours. Subsequently, PIA and eDNA were detected by dot blot and absorbance, respectively (71, 72).

Determination of *icaA* and *cidA* expression

The RNA of MRSA (by different treatments) was extracted and detected by a Q3000 Micro UV Spectrophotometer (Quawell, USA)

on the basis of the absorbance ratio of OD₂₆₀ to OD₂₈₀. RNA was then reverse-transcribed to cDNA by using HiScript IIQ RT Super Mix for qPCR (+gDNA wiper). The cDNA (100 ng) was analyzed by ChamQ Universal SYBR qPCR Master Mix, and qPCR was performed by the CFX Connect Real-Time System (Bio-Rad, CA, USA). The primer sequences corresponding to biofilm-related genes were obtained from the gene bank (<https://cipotato.org/genebankcip/>) and were synthesized by Tianyi Huiyuan Gene Technology Co., Ltd. (China). The primers were seen in table S2.

Accumulation and penetration observation of nanosystems into biofilms

The permeation and accumulation of three different nanosystems into biofilms were observed by using fluorescence from DAPI and nanosystems. As before, MSRA (10⁸ CFU ml⁻¹) was incubated in confocal culture dishes for 24 hours to form biofilms, and then the equivalent concentration of PCN-224, Arg-PCN, and Arg-PCN@Gel was added to interact with biofilms for different times before staining. After interaction for a fixed time, 1 ml of DAPI (20 μg ml⁻¹) was added for 25 min of staining, and then the stained biofilms were imaged by using a STORM super-resolution confocal scanning microscope (Nikon, Japan).

Living and dead MRSA determination inside biofilms

Mixed SYTO9 and PI dyes were used to observe the living/dead MRSA inside biofilms. As before, MSRA (10⁸ CFU ml⁻¹) was cultured in confocal culture dishes for 24 hours to form biofilms, and then equal volumes of different nanosystems were added to interact with biofilms for 24 hours for staining. After removing the culture medium and washing with PBS three times, 200 μl of mixed dyes were stained for 25 min, and then rinsed three times for 2 min each time. After staining, MRSA with intact membranes showed green fluorescence, while bacteria with damaged membrane structures showed red fluorescence. Then, the stained biofilms were imaged by a STORM super-resolution laser confocal scanning microscope (Nikon, Japan).

Destruction detection of biofilms

The lysostaphin sensitivity test, AKP kit, and ONPG hydrolysis test were used to reveal the biofilm damage by nanosystems. First, Mature biofilms were treated with different nanosystems with irradiation. The culture medium was collected and the supernatant was incubated with an AKP kit, and then the absorbance (OD₅₂₀) was detected by a UQuant microplate reader (BioTek Instruments, Inc., VT, USA). Second, the biofilms were collected by sonication and standardized (OD₆₀₀ = 0.1), and then incubated with lysostaphin (10 μg ml⁻¹) and ONPG solution (0.75 M NaH₂PO₄ buffer, pH 7), respectively. Last, the absorbance was measured at 600 and 420 nm by a UQuant microplate reader, respectively.

Persistent cell detection inside biofilms

Biofilms were treated with nanosystems and vancomycin (32 μg ml⁻¹) for 24 hours, respectively. After incubating for 2 hours, the light groups were irradiation for 30 min, and continued to be cultured. The biofilms were then collected on columbia blood agar plates to observe persistent cells and normal colonies (73, 74).

Target therapy experiments

All experiments were conducted in accordance with the approval of the Animal Care and Use Committee of Huazhong Agricultural University (Wuhan, China) (approval number: HZAUMO-2021-0185). Healthy 6- to 8-week-old male Balb/c mice and female Balb/c Nude mice (specific pathogen-free, 18 ± 2 g) were provided by the Laboratory Animal Center of Huazhong Agricultural University (Wuhan, China). To evaluate the targeting effect and anti-infection effect of nanosystems, the subcutaneous abscess model was established. Briefly, the right hindlimbs of the mice were shaved and injected subcutaneously with MRSA B1-1 (10⁸ CFU ml⁻¹, 100 μl). After inoculation for 24 hours, ruthenium red staining was used to confirm the formation of biofilm at the infected site of mice. Infected Balb/c Nude mice were given 100 μl of PCN-224, Arg-PCN, and Arg-PCN@Gel at 2 mg ml⁻¹ intravenously, and the distribution of nanosystems in mice was observed by IVIS Spectrum In Vivo Imaging System (PerkinElmer Ltd., MA, USA) after a certain period of time after injection.

The infected Balb/c mice were randomly divided into six groups (labels A to F, six mice per group), and 100 μl of vancomycin solution (45 mg kg⁻¹, setting up two groups of A and B), normal saline (groups C and D), and Arg-PCN@Gel (10 mg kg⁻¹, groups E and F) were administered by a single injection through the tail vein. Among them, groups A, C, and E were given daily irradiation treatment for 30 min at the infected site 1 day after administration, and the irradiation treatment was continued for 7 days. After 7 and 12 days of treatment, three mice per group were euthanized, and the infection tissues were collected and pressed on the nitrocellulose membrane for 30 s. The presence or absence of biofilms was confirmed by ruthenium red staining. The tissue was used for grinding and homogenization, and viable MRSA at the infection site was detected by the coating plate method after proper dilution. At the same time, the isolates isolated from the body were tested for MIC again. In addition, the abscess area was photographed at the established time to record wound change at the abscess site, and the size of the infection site was measured by calipers.

Cellular immunity test

The activated nutritional immunity of PCN-224, Arg-PCN, and Arg-PCN@Gel was determined by TNF-α, IL-4, iNOS, and Arg-1 ELISA kit. After complete adherent of RAW264.7 cells, it was infected with a density of 10⁸ CFUs MRSA per well for 12 hours. Then, PCN-224, Arg-PCN, and Arg-PCN@Gel were respectively added into the infected and normal cells to make the concentration of 8 μg ml⁻¹. Meanwhile, NaNO₂ (0.53 μM) and culture medium were used as NO and blank control, respectively. Under irradiation for 0 and 30 min, they were continued to culture for 6 and 24 hours and then the protein was collected by 200 μl of radioimmunoprecipitation assay lysis buffer with 1 mM phenylmethanesulfonyl fluoride. The NO concentration, bacterial colony, TNF-α, IL-4, iNOS, and Arg-1 in the cell lysate were determined.

Immunotherapy experiments

The infected Balb/c mice were divided into six groups (labels A to F, 12 mice per group) for single-dose treatment as above. After 1, 3, 7, and 12 days of treatment, three mice per group were euthanized and the infection tissues were collected to detect the immune factors (iNOS, Arg-1, TNF-α, IL-1β, IL-6, IL-4, and IL-10). The remaining

tissues were used for hematoxylin and eosin and CD₃₁ sections and observed by an optical microscope.

Transcriptomics

The MRSA biofilms untreated and treated by Arg-PCN@Gel for 30-min irradiation were used for the transcriptomic study. The whole-genome sequencing of B1-1 was performed before the transcriptomic study. Arg-PCN@Gel was added into mature biofilms to make the concentration of 4 $\mu\text{g ml}^{-1}$, incubated for 2 hours, irradiated for 30 min, and incubated for 24 hours. RNA-seq was performed by the Illumina platform of Nanjing Personal Gene Technology Co., Ltd (Nanjing, China). One percent agarose gel was used to monitor RNA degradation and contamination, and RNA Nano 6000 Assay Kit and Agilent Bioanalyzer 2100 system were used to assess RNA integrity. Genes with adjusted $P < 0.05$ identified by DESeq were considered differentially expressed. According to the KEGG analysis, differentially significant genes were assigned to different functional groups. Transcriptomics were verified by real-time qPCR (primers were seen in table S2).

Metabolic activity test

To study the effect of nanosystems on metabolic activity, resazurin was used. Briefly, control, NaNO₂, and nanosystem-treated MRSA were collected by centrifugation at 12,000 rpm for 15 min. The precipitates were resuspended in 1 ml of 0.9% saline. Then, $1/10$ volume of resazurin solution (3 mg ml^{-1}) was added to the cell suspension and incubated in the darkness at 37°C for 24 hours. After incubation, metabolic activity was analyzed by measuring the fluorescence intensity of control and treated cells at Ex/Em of 530/590 nm.

Steatolysis test

One hundred microliters of control, NaNO₂, and nanosystem-treated MRSA was added to 900 μl of lipase substrate [1 volume of a 0.3% disodium 4-nitrophenylphosphate 2-propanol solution and 9 volumes of tris-HCL buffer containing 0.2% sodium deoxycholate and 0.1% gum arabic (50 mM, pH 8.0)] and incubated at 37°C for 1 hour. The supernatant was then collected by centrifugation at 10,000 rpm for 10 min and the absorbance was read at 410 nm. The formula is as follows

$$\text{Lipase inhibition rate} = (\text{Control OD}_{410} - \text{treated OD}_{410}) / \text{Control OD}_{410}.$$

ATP detection

The biofilm treated with control, NaNO₂, and nanosystems was centrifuged at 8000 rpm for 2 min to collect, washed with sterile water three times to remove ATP outside the MRSA, and then tested according to the ATP detection kit.

$$\text{ATP inhibition rate} = (\text{Control OD}_{525} - \text{treated OD}_{525}) / \text{Control OD}_{525}.$$

Statistical analysis

All the experiments were performed in triplicate biological independent samples (means \pm SD, $n = 3$), except for Fig. 9H (means \pm SD, $n = 2$). Intergroup and intragroup comparison analyses in each experiment were calculated by analyses of variance

(ANOVAs) with the Duncan test. All statistical analyses were carried out by using SPSS (version 18.0). Probability $P < 0.05$ was considered statistically significant ($*P < 0.05$, $**P < 0.01$, and $***P < 0.001$).

Supplementary Materials

This PDF file includes:

Figs. S1 to S26

Tables S1 and S2

[View/request a protocol for this paper from Bio-protocol.](#)

REFERENCES AND NOTES

- Centers for Disease Control and Prevention, *Antibiotic Resistance Threats in the United States, 2019* (Centers for Disease Control and Prevention, 2019); www.cdc.gov/drugresistance/pdf/threats-report/2019-ar-threats-report-508.pdf
- D. Qu, Z. Hou, J. Li, L. Luo, S. Su, Z. Ye, Y. Bai, X. Zhang, G. Chen, Z. Li, Y. Wang, X. Xue, X. Luo, M. Li, A New coumarin compound DCH combats methicillin-resistant *Staphylococcus aureus* biofilm by targeting arginine repressor. *Sci. Adv.* **6**, eaay9597 (2020).
- H. Ji, K. Dong, Z. Yan, C. Ding, Z. Chen, J. Ren, X. Qu, Bacterial hyaluronidase self-triggered prodrug release for chemo-photothermal synergistic treatment of bacterial infection. *Small* **12**, 6200–6206 (2016).
- T. Oyama, M. Miyazaki, M. Yoshimura, T. Takata, H. Ohjimi, S. Jimi, Biofilm-forming methicillin-resistant *Staphylococcus aureus* survive in Kupffer cells and exhibit high virulence in mice. *Toxins* **8**, 198 (2016).
- X. Li, D. Chen, S. Xie, Current progress and prospects of organic nanoparticles against bacterial biofilm. *Adv. Colloid Interface Sci.* **294**, 102475 (2021).
- D. Davies, Understanding biofilm resistance to antibacterial agents. *Nat. Rev. Drug Discov.* **2**, 114–122 (2003).
- M. Sprenger, K. Fukuda, New mechanisms, new worries. *Science* **351**, 1263–1264 (2016).
- Z. Zhao, R. Yan, X. Yi, J. Li, J. Rao, Z. Guo, Y. Yang, W. Li, Y.-Q. Li, C. Chen, Bacteria-activated theranostic nanoprobes against methicillin-resistant *Staphylococcus aureus* infection. *ACS Nano* **11**, 4428–4438 (2017).
- R. Agarwal, C. T. Johnson, B. R. Imhoff, R. M. Donlan, N. A. Mc Carty, A. J. Garcia, Inhaled bacteriophage-loaded polymeric microparticles ameliorate acute lung infections. *Nat. Biomed. Eng.* **2**, 841–849 (2018).
- T. Shi, X. Hou, S. Guo, L. Zhang, C. Wei, T. Peng, X. Hu, Nanohole-boosted electron transport between nanomaterials and bacteria as a concept for nano–bio interactions. *Nat. Commun.* **12**, 493 (2021).
- M. Li, L. Li, K. Su, X. Liu, T. Zhang, Y. Liang, D. Jing, X. Yang, D. Zheng, Z. Cui, Z. Li, S. Zhu, K. W. K. Yeung, Y. Zheng, X. Wang, S. Wu, Highly effective and noninvasive near-infrared eradication of a *Staphylococcus aureus* Biofilm on Implants by a Photoresponsive Coating within 20 Min. *Adv. Sci.* **6**, 1900599 (2019).
- Y. Feng, C. C. Tonon, S. Ashraf, T. Hasan, Photodynamic and antibiotic therapy in combination against bacterial infections: Efficacy, determinants, mechanisms, and future perspectives. *Adv. Drug Deliv. Rev.* **177**, 113941 (2021).
- V.-N. Nguyen, Z. Zhao, B. Z. Tang, J. Yoon, Organic photosensitizers for antimicrobial phototherapy. *Chem. Soc. Rev.* **51**, 3324–3340 (2022).
- W. Wang, F. Wu, Q. Zhang, N. Zhou, M. Zhang, T. Zheng, Y. Li, B. Z. Tang, Aggregation-induced emission nanoparticles for single near-infrared light-triggered photodynamic and photothermal antibacterial therapy. *ACS Nano* **16**, 7961–7970 (2022).
- Y. Deng, F. Jia, S. Chen, Z. Shen, Q. Jin, G. Fu, J. Ji, Nitric oxide as an all-rounder for enhanced photodynamic therapy: Hypoxia relief, glutathione depletion and reactive nitrogen species generation. *Biomaterials* **187**, 55–65 (2018).
- L. Jun, S. Shuang, M. Jiashen, T. Lei, L. Xiangmei, Z. Yufeng, L. Zhaoyang, Y. K. W. Kwok, C. Zhenduo, L. Yanqin, Z. Shengli, Z. Xingcai, W. Shuilin, 2D MOF periodontitis photodynamic therapy. *J. Am. Chem. Soc.* **143**, 15427–15439 (2021).
- K. Ni, Z. Xu, A. Culbert, T. Luo, N. Guo, K. Yang, E. Pearson, B. Preusser, T. Wu, P. L. Riviere, R. R. Weichselbaum, M. T. Spiotto, W. Lin, Synergistic checkpoint-blockade and radiotherapy-radiodynamic therapy via an immunomodulatory nanoscale metal-organic framework. *Nat. Biomed. Eng.* **6**(2), 144–156 (2022).
- R. A. Proctor, A. Kriegerkorte, B. C. Kahl, K. Becker, B. Löffler, G. Peters, *Staphylococcus aureus* small colony variants (SCVs): A road map for the metabolic pathways involved in persistent infections. *Front. Cell. Infect. Microbiol.* **4**, 99 (2014).

19. T. R. McCulloch, T. J. Wells, F. Souza-Fonseca-Guimaraes, Towards efficient immunotherapy for bacterial infection. *Trends Microbiol.* **30**, 158–169 (2022).
20. X. Chen, Y. Yang, G. Ye, S. Liu, J. Liu, Chiral ruthenium nanozymes with self-cascade reaction driven the NO generation induced macrophage M1 polarization realizing the lung cancer "cocktail therapy". *Small* **8**, 2207823 (2023).
21. L. R. Thurlow, G. S. Joshi, J. R. Clark, J. S. Spontak, C. J. Neely, R. Maile, A. R. Richardson, Functional modularity of the arginine catabolic mobile element contributes to the success of USA300 methicillin-resistant *Staphylococcus aureus*. *Cell Host Microbe* **13**, 100–107 (2013).
22. T. Schön, M. Lerm, O. Stendahl, Shortening the 'short-course' therapy-insights into host immunity may contribute to new treatment strategies for tuberculosis. *J. Intern. Med.* **273**, 368–382 (2013).
23. J. Hou, Y. Pan, D. Zhu, Y. Fan, G. Feng, Y. Wei, H. Wang, K. Qin, T. Zhao, Q. Yang, Y. Zhu, Y. Che, Y. Liu, J. Cheng, D. Kong, P. G. Wang, J. Shen, Q. Zhao, Targeted delivery of nitric oxide via a 'bump-and-hole'-based enzyme-prodrug pair. *Nat. Chem. Biol.* **15**, 151–160 (2019).
24. D. O. Schairer, J. S. Chouake, J. D. Nosanchuk, A. J. Friedman, The potential of nitric oxide releasing therapies as antimicrobial agents. *Virulence* **3**, 271–279 (2012).
25. Y. Tang, T. Wang, J. Feng, F. Rong, K. Wang, P. Li, W. Huang, Photoactivatable nitric oxide-releasing gold nanocages for enhanced hyperthermia treatment of biofilm-associated infections. *ACS Appl. Mater. Interfaces* **13**, 50668–50681 (2021).
26. M. Wan, H. Chen, Q. Wang, Q. Niu, P. Xu, Y. Yu, T. Zhu, C. Mao, J. Shen, Bio-inspired nitric-oxide-driven nanomotor. *Nat. Commun.* **10**, 966 (2019).
27. C. Porayath, M. K. Suresh, R. Biswas, B. G. Nair, N. Mishra, S. Pal, Autolysin mediated adherence of *staphylococcus aureus* with fibronectin, gelatin and heparin. *Int. J. Biol. Macromol.* **110**, 179–184 (2018).
28. L.-L. Li, J.-H. Xu, G.-B. Qi, X. Zhao, F. Yu, H. Wang, Core-shell supramolecular gelatin nanoparticles for adaptive and "on-demand" antibiotic delivery. *ACS Nano* **8**, 4975–4983 (2014).
29. M. Toth, A. Sohail, R. Fridman, Assessment of gelatinases (MMP-2 and MMP-9) by gelatin zymography. *Methods Mol. Biol.* **878**, 121–135 (2012).
30. J. Park, Q. Jiang, D. Feng, L. Mao, H.-C. Zhou, Size-controlled synthesis of porphyrinic metal-organic framework and functionalization for targeted photodynamic therapy. *J. Am. Chem. Soc.* **138**, 3518–3525 (2016).
31. X. Nie, S. Wu, T. Hussain, Q. Wei, PCN-224 nanoparticle/polyacrylonitrile nanofiber membrane for light-driven bacterial inactivation. *Nanomaterials* **11**, 3162 (2021).
32. W. Dong, Z. Li, W. Wen, B. Liu, G. Wen, Novel CdS/MOF cathodic photoelectrochemical (PEC) platform for the detection of doxorubicin hydrochloride and gentamicin sulfate. *ACS Appl. Mater. Interfaces* **13**(48), 57497–57504 (2021).
33. Z. Zhang, R. Wang, R. Luo, J. Zhu, X. Huang, W. Liu, F. Liu, F. Feng, W. Qu, An activatable theranostic nanoprobe for dual-modal imaging-guided photodynamic therapy with self-reporting of sensitizer activation and therapeutic effect. *ACS Nano* **15**, 5366–5383 (2021).
34. H. Zhang, G. M. Annich, J. Miskulin, K. Stankiewicz, K. Osterholzer, S. I. Merz, R. H. Bartlett, M. E. Meyerhoff, Nitric oxide-releasing fumed silica particles: Synthesis, characterization, and biomedical application. *J. Am. Chem. Soc.* **125**, 5015–5024 (2003).
35. Y. Chen, S.-I. Roohani-Esfahani, Z. F. Lu, H. Zreiqat, C. R. Dunstan, Zirconium ions up-regulate the BMP/SMAD signaling pathway and promote the proliferation and differentiation of human osteoblasts. *PLOS ONE* **10**, e0113426 (2015).
36. M. Montazerian, B. E. Yekta, V. K. Marghussian, C. F. Bellani, R. L. Siqueira, E. D. Zanotto, Bioactivity and cell proliferation in radiopaque gel-derived CaO–P₂O₅–SiO₂–ZrO₂ glass and glass–ceramic powders. *Mater. Sci. Eng. C Mater. Biol. Appl.* **55**, 436–447 (2015).
37. M. B. da Cruz, J. F. Marques, B. F. Fernandes, S. Madeira, Ó. Carvalho, F. S. Silva, A. D. S. P. da Mata, J. M. M. Caramês, Peri-implant cell response on groove and pore-textured zirconia surfaces. *J. Oral. Biosci.* **64**, 100–107 (2022).
38. M. Tato, Y. López, M. I. Morosini, A. Moreno-Bofarull, F. Garcia-Alonso, D. Gargallo-Viola, J. Vila, R. Cantón, Characterization of variables that may influence ozenoxacin in susceptibility testing, including MIC and MBC Values. *Diagn. Microbiol. Infect. Dis.* **78**, 263–267 (2014).
39. X. Zhu, J. Guo, Y. Yang, J. Liu, Macrophage polarization induced by bacteria-responsive antibiotic-loaded nanozymes for multidrug resistance-bacterial infections management. *Small* **19**, e2204928 (2023).
40. K. Schilcher, A. R. Horswill, Staphylococcal biofilm development: Structure, regulation, and treatment strategies. *Microbiol. Mol. Biol. Rev.* **84**, e00026-19 (2020).
41. S. Gao, X. Yan, G. Xie, M. Zhu, X. Ju, P. J. Stang, Y. Tian, Z. Niu, Membrane intercalation-enhanced photodynamic inactivation of bacteria by a metallacycle and TAT-decorated virus coat protein. *Proc. Natl. Acad. Sci. U.S.A.* **116**, 23437–23443 (2019).
42. S. M. Jones, M. Morgan, T. J. Humphrey, H. Lappin-Scott, Effect of vancomycin and rifampicin on methicillin-resistant *Staphylococcus aureus* biofilms. *Lancet* **357**, 40–41 (2001).
43. C. Mottola, C. S. Matias, J. J. Mendes, J. Melo-Cristino, L. Tavares, P. Cavaco-Silva, M. Oliveira, Susceptibility patterns of *Staphylococcus aureus* biofilms in diabetic foot infections. *BMC Microbiol.* **16**, 119 (2016).
44. D. Lebeaux, A. Chauhan, S. Létoffé, F. Fischer, H. de Reuse, C. Beloin, J.-M. Ghigo, pH-mediated potentiation of aminoglycosides kills bacterial persisters and eradicates in vivo biofilms. *J. Infect. Dis.* **210**, 1357–1366 (2014).
45. K. P. Rumbaugh, K. Sauer, Biofilm dispersion. *Nat. Rev. Microbiol.* **18**, 571–586 (2020).
46. G. Nakagami, G. Schultz, D. J. Gibson, P. Phillips, A. Kitamura, T. Minematsu, T. Miyagaki, A. Hayashi, S. Sasaki, J. Sugama, H. Sanada, Biofilm detection by wound blotting can predict slough development in pressure ulcers: A prospective observational study. *Wound Repair Regen.* **25**, 131–138 (2017).
47. D. J. Elzi, W. E. Bauta, J. R. Sanchez, T. Das, S. Mogare, P. Z. Fatland, M. Iza, A. Pertsemilidis, V. I. Rebel, Identification of a novel mechanism for meso-tetra (4-carboxyphenyl) porphyrin (TCPP) uptake in cancer cells. *FASEB J.* **35**, e21427 (2021).
48. A. Zhang, K. Meng, Y. Liu, Y. Pan, W. Qu, D. Chen, S. Xie, Absorption, distribution, metabolism, and excretion of nanocarriers in vivo and their influences. *Adv. Colloid Interface Sci.* **284**, 102261 (2020).
49. Y. Liu, D. Huo, X. Zhu, X. Chen, A. Lin, Z. Jia, J. Liu, A ruthenium nanoframe/enzyme composite system as a self-activating cascade agent for the treatment of bacterial infections. *Nanoscale* **13**, 14900–14914 (2021).
50. X. Zhu, X. Chen, Z. Jia, D. Huo, Y. Liu, J. Liu, Cationic chitosan@Ruthenium dioxide hybrid nanozymes for photothermal therapy enhancing ROS-mediated eradicating multidrug resistant bacterial infection. *J. Colloid Interface Sci.* **603**, 615–632 (2021).
51. E. A. Gantwerker, D. B. Hom, Skin: Histology and physiology of wound healing. *Clin. Plast. Surg.* **39**, 85–97 (2012).
52. J. Satriano, Argmatine: At the crossroads of the arginine pathways. *Ann. N. Y. Acad. Sci.* **1009**, 34–43 (2003).
53. C. Bogdan, Nitric oxide and the immune response. *Nat. Immunol.* **2**, 907–916 (2001).
54. Z. Huang, Y. Zhang, X. Zheng, Z. Liu, D. Yao, Y. Zhao, X. Chen, J. J. Aweya, Functional characterization of arginine metabolic pathway enzymes in the antibacterial immune response of penaeid shrimp. *Dev. Comp. Immunol.* **127**, 104293 (2022).
55. G. Ji, S. Silver, Reduction of arsenate to arsenite by the ArsC protein of the arsenic resistance operon of *Staphylococcus aureus* plasmid Pl258. *Proc. Natl. Acad. Sci. U.S.A.* **89**, 9474–9478 (1992).
56. A. Lin, Y. Liu, X. Zhu, X. Chen, J. Liu, Y. Zhou, X. Qin, J. Liu, Bacteria-responsive biomimetic selenium nanosystem for multidrug-resistant bacterial infection detection and inhibition. *ACS Nano* **13**, 13965–13984 (2019).
57. G. Guo, H. Zhang, H. Shen, C. Zhu, R. He, J. Tang, Y. Wang, X. Jiang, J. Wang, W. Bu, X. Zhang, Space-selective chemodynamic therapy of CuFe₂O₈ Nanocubes for implant-related infections. *ACS Nano* **14**, 13391–13405 (2020).
58. X. Liao, H. Li, Y. Guo, F. Yang, Y. Chen, X. He, H. Li, W. Xia, Z.-W. Mao, H. Sun, Regulation of DNA-binding activity of the *Staphylococcus aureus* catabolite control protein a by copper (II)-Mediated Oxidation. *J. Biol. Chem.* **298**, 101587 (2022).
59. H. Peng, J. Shen, K. A. Edmonds, J. L. Luebke, A. K. Hickey, L. D. Palmer, F.-M. J. Chang, K. A. Bruce, T. E. Kehl-Fie, E. P. Skaar, D. P. Giedroc, Sulfide homeostasis and nitroxyl intersect via formation of reactive sulfur species in *Staphylococcus aureus*. *mSphere* **2**, e00082-17 (2017).
60. E. Tarrant, G. P. Riboldi, M. R. McIlvin, J. Stevenson, A. Barwinska-Sendra, L. J. Stewart, M. A. Saito, K. J. Waldron, Copper stress in *Staphylococcus aureus* leads to adaptive changes in central carbon metabolism. *Metallomics* **11**, 183–200 (2019).
61. M. A. Kohanski, D. J. Dwyer, B. Hayete, C. A. Lawrence, J. J. Collins, A common mechanism of cellular death induced by bactericidal antibiotics. *Cell* **130**, 797–810 (2007).
62. J. Messens, J. C. Martins, E. Brosens, K. Van Belle, D. M. Jacobs, R. Willem, L. Wyns, Kinetics and active site dynamics of *Staphylococcus aureus* arsenate reductase. *J. Biol. Inorg. Chem.* **7**, 146–156 (2002).
63. C. Li, F. Sun, H. Cho, Y. Yelavarthi, C. Sohn, C. He, O. Schneewind, T. Bae, CcpA mediates proline auxotrophy and is required for *Staphylococcus aureus* pathogenesis. *J. Bacteriol.* **192**, 3883–3892 (2010).
64. L. L. Bulock, J. Ahn, D. Shinde, S. Pandey, C. Sarmiento, V. C. Thomas, C. Guda, K. W. Bayles, M. R. Sadykov, Interplay of CodY and CcpA in regulating central metabolism and biofilm formation in *Staphylococcus aureus*. *J. Bacteriol.* **204**, e0061721 (2022).
65. Z. DeMars, J. L. Bose, Redirection of metabolism in response to fatty acid kinase in *Staphylococcus aureus*. *J. Bacteriol.* **200**, e00345-18 (2018).
66. K. L. James, A. B. Mogen, J. N. Brandwein, S. S. Orsini, M. J. Ridder, M. A. Markiewicz, J. L. Bose, K. C. Rice, *Staphylococcus aureus* Interplay of nitric oxide synthase (NOS) and SrrAB in modulation of metabolism and virulence. *Infect. Immun.* **87**, (2019).
67. A. Valliammai, S. Sethupathy, S. Ananthi, A. Priya, A. Selvaraj, V. Nivetha, C. Aravindraj, S. Mahalingam, S. K. Pandian, Proteomic profiling unveils citral modulating expression of

- IsaA, CodY and SaeS to inhibit biofilm and virulence in methicillin-resistant *Staphylococcus aureus*. *Int. J. Biol. Macromol.*, (2020).
68. A. A. Mashruwala, A. van de Guchte, J. M. Boyd, Impaired respiration elicits SrrAB-dependent programmed cell lysis and biofilm formation in *Staphylococcus aureus*. *eLife* **6**, e23845 (2017).
69. D. Wang, L. Niu, Z.-Y. Qiao, D.-B. Cheng, J. Wang, Y. Zhong, F. Bai, H. Wang, H. Fan, Synthesis of self-assembled porphyrin nanoparticle photosensitizers. *ACS Nano* **12**(4), 3796–3803 (2018).
70. H. Mu, F. Guo, H. Niu, Q. Liu, S. Wang, J. Duan, Chitosan improves anti-biofilm efficacy of gentamicin through facilitating antibiotic penetration. *Int. J. Mol. Sci.* **15**, 22296–22308 (2014).
71. S. Schlag, C. Nerz, T. A. Birkenstock, F. Altenberend, F. Götz, Inhibition of staphylococcal biofilm formation by nitrite. *J. Bacteriol.* **189**, 7911–7919 (2007).
72. K. C. Rice, E. E. Mann, J. L. Endres, E. C. Weiss, J. E. Cassat, M. S. Smeltzer, K. W. Bayles, The *cidA* murein hydrolase regulator contributes to DNA release and biofilm development in *Staphylococcus aureus*. *Proc. Natl. Acad. Sci. U.S.A.* **104**(19), 8113–8118 (2007).
73. B. C. Kahl, K. Becker, B. Löffler, Clinical significance and pathogenesis of staphylococcal small colony variants in persistent infections. *Clin. Microbiol. Rev.* **29**, 401–427 (2016).
74. C. von Eiff, G. Peters, K. Becker, The small colony variant (SCV) concept — The role of staphylococcal SCVs in persistent infections. *Injury* **37**, S26–S33 (2006).

Acknowledgments: This work was supported by the National Natural Science Foundation of China (grant no. 32273064), National Key Research and Development Program of China (2022YFD1300705), and Project 2662023DKPY004 supported by the Fundamental Research Funds for the Central Universities. **Author contributions:** Conceptualization: A.Z., D.C., and S.X. Methodology: A.Z., D.C., and S.X. Investigation: A.Z., H.W., and X.C. Visualization: A.Z. and Z.C. Supervision: Y.P., W.Q., H.H., D.C., and S.X. Writing—original draft: A.Z. Writing—review and editing: D.C. and S.X. **Competing interests:** The authors declare that they have no competing interests. **Data and materials availability:** All data needed to evaluate the conclusions in the paper are present in the paper and/or the Supplementary Materials.

Submitted 30 January 2023

Accepted 9 June 2023

Published 14 July 2023

10.1126/sciadv.adg9116